Systematic study of nuclear effects in $p+$Al, $p+$Au, $d+$Au, and ^{3}He $+$ Au collisions at $\sqrt{s_{NN}} = 200$ GeV using π^0 production

U. A. Acharya,[23] A. Adare,[12] C. Aidala,[46,47] N. N. Ajitanand,[69,*] Y. Akiba,[63,64,†] H. Al-Bataineh,[55] J. Alexander,[69] M. Alfred,[25] V. Andrieux,[47] A. Angerami,[13] K. Aoki,[34,37,63] N. Apadula,[30,70] Y. Aramaki,[11,63] H. Asano,[37,63] E. T. Atomssa,[38] R. Averbeck,[70] T. C. Awes,[58] B. Azmoun,[7] V. Babintsev,[26] M. Bai,[6] G. Baksay,[21] L. Baksay,[21] N. S. Bandara,[46] B. Bannier,[70] K. N. Barish,[8] B. Bassalleck,[54] A. T. Basye,[1] S. Bathe,[5,8,64] V. Baublis,[61] C. Baumann,[7,48] A. Bazilevsky,[7] M. Beaumier,[8] S. Beckman,[12] S. Belikov,[7,*] R. Belmont,[12,47,56,76] R. Bennett,[70] A. Berdnikov,[66] Y. Berdnikov,[66] J. H. Bhom,[80] L. Bichon,[76] B. Blankenship,[76] D. S. Blau,[36,53] J. S. Bok,[55,80] V. Borisov,[66] K. Boyle,[64,70] M. L. Brooks,[41] J. Bryslawskyj,[5,8] H. Buesching,[7] V. Bumazhnov,[26] G. Bunce,[7,64] S. Butsyk,[41] S. Campbell,[13,30,70] V. Canoa Roman,[70] A. Caringi,[49] R. Cervantes,[70] C.-H. Chen,[64,70] M. Chiu,[7] C. Y. Chi,[13] I. J. Choi,[27,80] J. B. Choi,[32,*] R. K. Choudhury,[4] P. Christiansen,[43] T. Chujo,[75] P. Chung,[69] O. Chvala,[8] V. Cianciolo,[58] Z. Citron,[70,78] B. A. Cole,[13] Z. Conesa del Valle,[38] M. Connors,[23,64,70] R. Corliss,[70] Y. Corrales Morales,[41] N. Cronin,[49,70] T. Csörgő,[18,79] M. Csanád,[17] L. D'Orazio,[45] T. Dahms,[70] S. Dairaku,[37,63] I. Danchev,[76] T. W. Danley,[57] K. Das,[22] A. Datta,[46,54] M. S. Daugherity,[1] G. David,[7,70] M. K. Dayananda,[23] C. T. Dean,[41] K. DeBlasio,[54] K. Dehmelt,[70] A. Denisov,[26] A. Deshpande,[64,70] E. J. Desmond,[7] K. V. Dharmawardane,[55] O. Dietzsch,[67] A. Dion,[30,70] P. B. Diss,[45] D. Dixit,[70] M. Donadelli,[67] J. H. Do,[80] V. Doomra,[70] O. Drapier,[38] A. Drees,[70] K. A. Drees,[6] J. M. Durham,[41,70] A. Durum,[26] D. Dutta,[4] S. Edwards,[22] Y. V. Efremenko,[58] F. Ellinghaus,[12] H. En'yo,[63,64] T. Engelmore,[13] A. Enokizono,[58,63,65] R. Esha,[70] S. Esumi,[75] B. Fadem,[49] W. Fan,[70] N. Feege,[70] D. E. Fields,[54] M. Finger, Jr.,[9] M. Finger,[9] D. Fitzgerald,[47] F. Fleuret,[38] S. L. Fokin,[36] Z. Fraenkel,[78,*] J. E. Frantz,[57,70] A. Franz,[7] A. D. Frawley,[22] K. Fujiwara,[63] Y. Fukao,[63] Y. Fukuda,[75] T. Fusayasu,[51] P. Gallus,[14] C. Gal,[70] P. Garg,[3,70] I. Garishvili,[40,72] H. Ge,[70] M. Giles,[70] F. Giordano,[27] A. Glenn,[40] H. Gong,[70] M. Gonin,[38] Y. Goto,[63,64] R. Granier de Cassagnac,[38] N. Grau,[2,13] S. V. Greene,[76] G. Grim,[41] M. Grosse Perdekamp,[27] T. Gunji,[11] H. Guragain,[23] H.-Å. Gustafsson,[43,*] T. Hachiya,[52,63,64] J. S. Haggerty,[7] K. I. Hahn,[19] H. Hamagaki,[11] J. Hamblen,[72] H. F. Hamilton,[1] J. Hanks,[13,70] R. Han,[60] S. Y. Han,[19,35] M. Harvey,[73] S. Hasegawa,[31] T. O. S. Haseler,[23] K. Hashimoto,[63,65] E. Haslum,[43] R. Hayano,[11] M. Heffner,[40] T. K. Hemmick,[70] T. Hester,[8] X. He,[23] J. C. Hill,[30] K. Hill,[12] A. Hodges,[23] M. Hohlmann,[21] R. S. Hollis,[8] W. Holzmann,[13] K. Homma,[24] B. Hong,[35] T. Horaguchi,[24] D. Hornback,[72] T. Hoshino,[24] N. Hotvedt,[30] J. Huang,[7] T. Ichihara,[63,64] R. Ichimiya,[63] Y. Ikeda,[75] K. Imai,[31,37,63] M. Inaba,[75] A. Iordanova,[8] D. Isenhower,[1] M. Ishihara,[63] M. Issah,[76] D. Ivanishchev,[61] Y. Iwanaga,[24] B. V. Jacak,[70] M. Jezghani,[23] X. Jiang,[41] J. Jin,[13] Z. Ji,[70] B. M. Johnson ®,[7,23] T. Jones,[1] K. S. Joo,[50] D. Jouan,[59] D. S. Jumper,[1,27] F. Kajihara,[11] J. Kamin,[70] S. Kanda,[11] J. H. Kang,[80] D. Kapukchyan,[8] J. Kapustinsky,[41] K. Karatsu,[37,63] S. Karthas,[70] M. Kasai,[63,65] D. Kawall,[46,64] M. Kawashima,[63,65] A. V. Kazantsev,[36] T. Kempel,[30] J. A. Key,[54] V. Khachatryan,[70] A. Khanzadeev,[61] A. Khatiwada,[41] K. M. Kijima,[24] J. Kikuchi,[77] B. Kimelman,[49] A. Kim,[19] B. I. Kim,[35] C. Kim,[8,35] D. J. Kim,[33] E.-J. Kim,[32] G. W. Kim,[19] M. Kim,[68] T. Kim,[19] Y.-J. Kim,[27] D. Kincses,[17] A. Kingan,[70] E. Kinney,[12] Á. Kiss,[17] E. Kistenev,[7] R. Kitamura,[11] J. Klatsky,[22] D. Kleinjan,[8] P. Kline,[70] T. Koblesky,[12] L. Kochenda,[61] B. Komkov,[61] M. Konno,[75] J. Koster,[27] D. Kotov,[61,66] A. Král,[14] A. Kravitz,[13] S. Kudo,[75] G. J. Kunde,[41] K. Kurita,[63,65] M. Kurosawa,[63,64] Y. Kwon,[80] G. S. Kyle,[55] Y. S. Lai,[13] J. G. Lajoie,[30] D. Larionova,[66] A. Lebedev,[30] D. M. Lee,[41] J. Lee,[19,71] K. B. Lee,[35] K. S. Lee,[35] S. Lee,[80] S. H. Lee,[30,47,70] M. J. Leitch,[41] M. A. L. Leite,[67] Y. H. Leung,[70] N. A. Lewis,[47] T. Liška,[14] P. Lichtenwalner,[49] P. Liebing,[64] S. H. Lim,[41,62,80] L. A. Linden Levy,[12] H. Liu,[41] M. X. Liu,[41] X. Li,[10] X. Li,[41] V.-R. Loggins,[27] D. A. Loomis,[47] K. Lovasz,[16] B. Love,[76] D. Lynch,[7] S. Lökös,[17] C. F. Maguire,[76] T. Majoros,[16] Y. I. Makdisi,[6] M. Makek,[81] M. D. Malik,[54] A. Manion,[70] V. I. Manko,[36] E. Mannel,[7,13] Y. Mao,[60,63] H. Masui,[75] F. Matathias,[13] M. McCumber,[41,70] P. L. McGaughey,[41] D. McGlinchey,[12,22,41] C. McKinney,[27] N. Means,[70] A. Meles,[55] M. Mendoza,[8] B. Meredith,[27] Y. Miake,[75] T. Mibe,[34] A. C. Mignerey,[45] K. Miki,[63,75] A. Milov,[7,78] D. K. Mishra,[4] J. T. Mitchell,[7] M. Mitrankova,[66] Iu. Mitrankov,[66] G. Mitsuka,[34,64] S. Miyasaka,[63,74] S. Mizuno,[63,75] A. K. Mohanty,[4] M. M. Mondal,[70] P. Montuenga,[27] H. J. Moon,[50] T. Moon,[35,80] Y. Morino,[11] A. Morreale,[8] D. P. Morrison,[7] T. V. Moukhanova,[36] B. Mulilo,[35,63] T. Murakami,[37,63] J. Murata,[63,65] A. Mwai,[69] K. Nagai,[74] S. Nagamiya,[34,63] K. Nagashima,[24] T. Nagashima,[65] J. L. Nagle,[12] M. Naglis,[78] M. I. Nagy,[17,79] I. Nakagawa,[63,64] H. Nakagomi,[63,75] Y. Nakamiya,[24] K. R. Nakamura,[37,63] T. Nakamura,[63] K. Nakano,[63,74] S. Nam,[19] C. Nattrass,[72] S. Nelson,[20] P. K. Netrakanti,[4] J. Newby,[40] M. Nguyen,[70] M. Nihashi,[24] T. Niida,[75] S. Nishimura,[11] R. Nouicer,[7,64] T. Novák,[18,79] N. Novitzky,[33,70,75] G. Nukazuka,[63,64] A. S. Nyanin,[36] E. O'Brien,[7] C. Oakley,[23] S. X. Oda,[11] C. A. Ogilvie,[30] K. Okada,[64] M. Oka,[75] Y. Onuki,[63] J. D. Orjuela Koop,[12] J. D. Osborn,[47,58] A. Oskarsson,[43] G. J. Ottino,[54] M. Ouchida,[24,63] K. Ozawa,[11,34,75] R. Pak,[7] V. Pantuev,[28,70] V. Papavassiliou,[55] I. H. Park,[19,71] J. S. Park,[68] S. Park,[63,68,70] S. K. Park,[35] W. J. Park,[35] M. Patel,[30] S. F. Pate,[55] H. Pei,[30] J.-C. Peng,[27] W. Peng,[76] H. Pereira,[15] D. V. Perepelitsa,[7,12] G. D. N. Perera,[55] D.Yu. Peressounko,[36] C. E. PerezLara,[70] J. Perry,[30] R. Petti,[7,70] M. Phipps,[7,27] C. Pinkenburg,[7] R. Pinson,[1] R. P. Pisani,[7]

---

[*]Deceased.

[†]Corresponding author: akiba@rcf.rhic.bnl.gov

M. Potekhin,[7] M. Proissl,[70] A. Pun,[57] M. L. Purschke,[7] H. Qu,[23] P. V. Radzevich,[66] J. Rak,[33] N. Ramasubramanian,[70] B. J. Ramson,[47] I. Ravinovich,[78] K. F. Read,[58,72] S. Rembeczki,[21] K. Reygers,[48] D. Reynolds,[69] V. Riabov,[53,61] Y. Riabov,[61,66] E. Richardson,[45] D. Richford,[5] T. Rinn,[27,30] D. Roach,[76] G. Roche,[42,*] S. D. Rolnick,[8] M. Rosati,[30] S. S. E. Rosendahl,[43] C. A. Rosen,[12] Z. Rowan,[5] P. Ružička,[29] J. G. Rubin,[47] J. Runchey,[30] A. S. Safonov,[66] B. Sahlmueller,[48,70] N. Saito,[34] T. Sakaguchi,[7] K. Sakashita,[63,74] H. Sako,[31] V. Samsonov,[53,61] S. Sano,[11,77] M. Sarsour,[23] S. Sato,[31,34] T. Sato,[75] S. Sawada,[34] B. Schaefer,[76] B. K. Schmoll,[72] K. Sedgwick,[8] J. Seele,[12] R. Seidl,[27,63,64] A. Sen,[30,72] R. Seto,[8] P. Sett,[4] A. Sexton,[45] D. Sharma,[70,78] I. Shein,[26] M. Shibata,[52] T.-A. Shibata,[63,74] K. Shigaki,[24] M. Shimomura,[30,52,75] T. Shioya,[75] K. Shoji,[37,63] P. Shukla,[4] A. Sickles,[7,27] C. L. Silva,[30,41] D. Silvermyr,[43,58] C. Silvestre,[15] K. S. Sim,[35] B. K. Singh,[3] C. P. Singh,[3] V. Singh,[3] M. Slunečka,[9] K. L. Smith,[22] M. Snowball,[41] R. A. Soltz,[40] W. E. Sondheim,[41] S. P. Sorensen,[72] I. V. Sourikova,[7] P. W. Stankus,[58] E. Stenlund,[43] M. Stepanov,[46,55,*] S. P. Stoll,[7] T. Sugitate,[24] A. Sukhanov,[7] T. Sumita,[63] J. Sun,[70] Z. Sun,[16] J. Sziklai,[79] E. M. Takagui,[67] R. Takahama,[52] A. Taketani,[63,64] R. Tanabe,[75] Y. Tanaka,[51] S. Taneja,[70] K. Tanida,[31,37,63,64,68] M. J. Tannenbaum,[7] S. Tarafdar,[3,76,78] A. Taranenko,[53,69] G. Tarnai,[16] H. Themann,[70] D. Thomas,[1] T. L. Thomas,[54] R. Tieulent,[23,44] A. Timilsina,[30] T. Todoroki,[63,64,75] M. Togawa,[64] A. Toia,[70] L. Tomášek,[29] M. Tomášek,[14,29] H. Torii,[24] C. L. Towell,[1] R. Towell,[1] R. S. Towell,[1] I. Tserruya,[78] Y. Tsuchimoto,[24] Y. Ueda,[24] B. Ujvari,[16] R. Vértesi,[79] C. Vale,[7] H. Valle,[76] H. W. van Hecke,[41] E. Vazquez-Zambrano,[13] A. Veicht,[13,27] J. Velkovska,[76] M. Virius,[14] V. Vrba,[14,29] N. Vukman,[81] E. Vznuzdaev,[61] X. R. Wang,[55,64] D. Watanabe,[24] K. Watanabe,[75] Y. Watanabe,[63,64] Y. S. Watanabe,[11,34] F. Wei,[30,55] R. Wei,[69] J. Wessels,[48] A. S. White,[47] S. N. White,[7] D. Winter,[13] C. P. Wong,[23,41] C. L. Woody,[7] R. M. Wright,[1] M. Wysocki,[12,58] B. Xia,[57] L. Xue,[23] C. Xu,[55] Q. Xu,[76] S. Yalcin,[70] Y. L. Yamaguchi,[11,63,70] H. Yamamoto,[75] K. Yamaura,[24] R. Yang,[27] A. Yanovich,[26] J. Ying,[23] S. Yokkaichi,[63,64] I. Yoon,[68] J. H. Yoo,[35] G. R. Young,[58] I. Younus,[39,54] Z. You,[60] I. E. Yushmanov,[36] H. Yu,[55,60] W. A. Zajc,[13] A. Zelenski,[6] S. Zhou,[10] and L. Zou[8]

(PHENIX Collaboration)

[1]*Abilene Christian University, Abilene, Texas 79699, USA*
[2]*Department of Physics, Augustana University, Sioux Falls, South Dakota 57197, USA*
[3]*Department of Physics, Banaras Hindu University, Varanasi 221005, India*
[4]*Bhabha Atomic Research Centre, Bombay 400 085, India*
[5]*Baruch College, City University of New York, New York, New York 10010, USA*
[6]*Collider-Accelerator Department, Brookhaven National Laboratory, Upton, New York 11973-5000, USA*
[7]*Physics Department, Brookhaven National Laboratory, Upton, New York 11973-5000, USA*
[8]*University of California-Riverside, Riverside, California 92521, USA*
[9]*Charles University, Ovocný trh 5, Praha 1, 116 36, Prague, Czech Republic*
[10]*Science and Technology on Nuclear Data Laboratory, China Institute of Atomic Energy, Beijing 102413, People's Republic of China*
[11]*Center for Nuclear Study, Graduate School of Science, University of Tokyo, 7-3-1 Hongo, Bunkyo, Tokyo 113-0033, Japan*
[12]*University of Colorado, Boulder, Colorado 80309, USA*
[13]*Columbia University, New York, New York 10027 and Nevis Laboratories, Irvington, New York 10533, USA*
[14]*Czech Technical University, Zikova 4, 166 36 Prague 6, Czech Republic*
[15]*Dapnia, CEA Saclay, F-91191, Gif-sur-Yvette, France*
[16]*Debrecen University, H-4010 Debrecen, Egyetem tér 1, Hungary*
[17]*ELTE, Eötvös Loránd University, H-1117 Budapest, Pázmány P. s. 1/A, Hungary*
[18]*Eszterházy Károly University, Károly Róbert Campus, H-3200 Gyöngyös, Mátrai út 36, Hungary*
[19]*Ewha Womans University, Seoul 120-750, Korea*
[20]*Florida A&M University, Tallahassee, Florida 32307, USA*
[21]*Florida Institute of Technology, Melbourne, Florida 32901, USA*
[22]*Florida State University, Tallahassee, Florida 32306, USA*
[23]*Georgia State University, Atlanta, Georgia 30303, USA*
[24]*Hiroshima University, Kagamiyama, Higashi-Hiroshima 739-8526, Japan*
[25]*Department of Physics and Astronomy, Howard University, Washington, DC 20059, USA*
[26]*IHEP Protvino, State Research Center of Russian Federation, Institute for High Energy Physics, Protvino, 142281, Russia*
[27]*University of Illinois at Urbana-Champaign, Urbana, Illinois 61801, USA*
[28]*Institute for Nuclear Research of the Russian Academy of Sciences, prospekt 60-letiya Oktyabrya 7a, Moscow 117312, Russia*
[29]*Institute of Physics, Academy of Sciences of the Czech Republic, Na Slovance 2, 182 21 Prague 8, Czech Republic*
[30]*Iowa State University, Ames, Iowa 50011, USA*
[31]*Advanced Science Research Center, Japan Atomic Energy Agency, 2-4 Shirakata Shirane, Tokai-mura, Naka-gun, Ibaraki-ken 319-1195, Japan*
[32]*Jeonbuk National University, Jeonju, 54896, Korea*
[33]*Helsinki Institute of Physics and University of Jyväskylä, P.O. Box 35, FI-40014 Jyväskylä, Finland*
[34]*KEK, High Energy Accelerator Research Organization, Tsukuba, Ibaraki 305-0801, Japan*
[35]*Korea University, Seoul 02841, Korea*
[36]*National Research Center "Kurchatov Institute," Moscow, 123098, Russia*

[37]*Kyoto University, Kyoto 606-8502, Japan*
[38]*Laboratoire Leprince-Ringuet, Ecole Polytechnique, CNRS-IN2P3, Route de Saclay, F-91128, Palaiseau, France*
[39]*Physics Department, Lahore University of Management Sciences, Lahore 54792, Pakistan*
[40]*Lawrence Livermore National Laboratory, Livermore, California 94550, USA*
[41]*Los Alamos National Laboratory, Los Alamos, New Mexico 87545, USA*
[42]*LPC, Université Blaise Pascal, CNRS-IN2P3, Clermont-Fd, 63177 Aubiere Cedex, France*
[43]*Department of Physics, Lund University, Box 118, SE-221 00 Lund, Sweden*
[44]*IPNL, CNRS/IN2P3, University Lyon, Université Lyon 1, F-69622, Villeurbanne, France*
[45]*University of Maryland, College Park, Maryland 20742, USA*
[46]*Department of Physics, University of Massachusetts, Amherst, Massachusetts 01003-9337, USA*
[47]*Department of Physics, University of Michigan, Ann Arbor, Michigan 48109-1040, USA*
[48]*Institut für Kernphysik, University of Münster, D-48149 Münster, Germany*
[49]*Muhlenberg College, Allentown, Pennsylvania 18104-5586, USA*
[50]*Myongji University, Yongin, Kyonggido 449-728, Korea*
[51]*Nagasaki Institute of Applied Science, Nagasaki-shi, Nagasaki 851-0193, Japan*
[52]*Nara Women's University, Kita-uoya Nishi-machi Nara 630-8506, Japan*
[53]*National Research Nuclear University, MEPhI, Moscow Engineering Physics Institute, Moscow, 115409, Russia*
[54]*University of New Mexico, Albuquerque, New Mexico 87131, USA*
[55]*New Mexico State University, Las Cruces, New Mexico 88003, USA*
[56]*Physics and Astronomy Department, University of North Carolina at Greensboro, Greensboro, North Carolina 27412, USA*
[57]*Department of Physics and Astronomy, Ohio University, Athens, Ohio 45701, USA*
[58]*Oak Ridge National Laboratory, Oak Ridge, Tennessee 37831, USA*
[59]*IPN-Orsay, University Paris-Sud, CNRS/IN2P3, Université Paris-Saclay, BP1, F-91406, Orsay, France*
[60]*Peking University, Beijing 100871, People's Republic of China*
[61]*PNPI, Petersburg Nuclear Physics Institute, Gatchina, Leningrad Region, 188300, Russia*
[62]*Pusan National University, Pusan 46241, Korea*
[63]*RIKEN Nishina Center for Accelerator-Based Science, Wako, Saitama 351-0198, Japan*
[64]*RIKEN BNL Research Center, Brookhaven National Laboratory, Upton, New York 11973-5000, USA*
[65]*Physics Department, Rikkyo University, 3-34-1 Nishi-Ikebukuro, Toshima, Tokyo 171-8501, Japan*
[66]*Saint Petersburg State Polytechnic University, St. Petersburg, 195251, Russia*
[67]*Universidade de São Paulo, Instituto de Física, Caixa Postal 66318, São Paulo CEP05315-970, Brazil*
[68]*Department of Physics and Astronomy, Seoul National University, Seoul 151-742, Korea*
[69]*Chemistry Department, Stony Brook University, SUNY, Stony Brook, New York 11794-3400, USA*
[70]*Department of Physics and Astronomy, Stony Brook University, SUNY, Stony Brook, New York 11794-3800, USA*
[71]*Sungkyunkwan University, Suwon, 440-746, Korea*
[72]*University of Tennessee, Knoxville, Tennessee 37996, USA*
[73]*Texas Southern University, Houston, Texas 77004, USA*
[74]*Department of Physics, Tokyo Institute of Technology, Oh-okayama, Meguro, Tokyo 152-8551, Japan*
[75]*Tomonaga Center for the History of the Universe, University of Tsukuba, Tsukuba, Ibaraki 305, Japan*
[76]*Vanderbilt University, Nashville, Tennessee 37235, USA*
[77]*Waseda University, Advanced Research Institute for Science and Engineering, 17 Kikui-cho, Shinjuku-ku, Tokyo 162-0044, Japan*
[78]*Weizmann Institute, Rehovot 76100, Israel*
[79]*Institute for Particle and Nuclear Physics, Wigner Research Centre for Physics, Hungarian Academy of Sciences (Wigner RCP, RMKI) H-1525 Budapest 114, POBox 49, Budapest, Hungary*
[80]*Yonsei University, IPAP, Seoul 120-749, Korea*
[81]*Department of Physics, Faculty of Science, University of Zagreb, Bijenička c. 32 HR-10002 Zagreb, Croatia*

The PHENIX Collaboration presents a systematic study of inclusive π^0 production from $p + p$, $p + $ Al, $p + $ Au, $d + $ Au, and ^{3}He $ + $ Au collisions at $\sqrt{s_{NN}} = 200$ GeV. Measurements were performed with different centrality selections as well as the total inelastic, 0–100%, selection for all collision systems. For 0–100% collisions, the nuclear-modification factors, R_{xA}, are consistent with unity for p_T above 8 GeV/c, but exhibit an enhancement in peripheral collisions and a suppression in central collisions. The enhancement and suppression characteristics are similar for all systems for the same centrality class. It is shown that for high-p_T-π^0 production, the nucleons in the d and ^{3}He interact mostly independently with the Au nucleus and that the counterintuitive centrality dependence is likely due to a physical correlation between multiplicity and the presence of a hard scattering process. These observations disfavor models where parton energy loss has a significant contribution

to nuclear modifications in small systems. Nuclear modifications at lower p_T resemble the Cronin effect—an increase followed by a peak in central or inelastic collisions and a plateau in peripheral collisions. The peak height has a characteristic ordering by system size as $p + \mathrm{Au} > d + \mathrm{Au} > {}^3\mathrm{He} + \mathrm{Au} > p + \mathrm{Al}$. For collisions with Au ions, current calculations based on initial-state cold nuclear matter effects result in the opposite order, suggesting the presence of other contributions to nuclear modifications, in particular at lower p_T.

I. INTRODUCTION

Measurements of transverse-momentum (p_T) distributions of particles produced in hadronic collisions are commonly used to obtain information from the interaction. At the Relativistic Heavy Ion Collider (RHIC) at Brookhaven National Laboratory, studies of the nuclear-modification factor R_{AA} of hadrons, defined as the ratio of the hadron yield per binary nucleon-nucleon collision in a given $A + A$ system to the yield measured in $p + p$ collisions, have led to significant insights. The discovery of the suppression of high-p_T neutral pions and charged hadrons [1,2] in $\mathrm{Au} + \mathrm{Au}$ collisions relative to scaled $p + p$ collisions at the same energy, was one of the first hints of parton energy loss in the strongly coupled quark gluon plasma (QGP). The apparent absence of any suppression in reference spectra from $d + \mathrm{Au}$ collisions [3,4], where the formation of QGP was not expected, was critical to establish parton energy loss as the origin of the observed suppression in $\mathrm{Au} + \mathrm{Au}$ collisions. The subsequent systematic studies of the suppression pattern of π^0 production in $\mathrm{Au} + \mathrm{Au}$ collisions at $\sqrt{s_{NN}} = 200$ GeV allowed for quantitative constraints on the medium transport coefficients [5,6].

Experimentally, evidence for cold-nuclear-matter effects was first observed in the late 1970s when the ratio of the production cross sections of hadrons from $p + \mathrm{A}$ to $p + p$ was found to vary with p_T [7,8]. This variation was referred to as the "Cronin effect": a suppression at low p_T followed by an enhancement around 2–5 GeV/c that vanishes toward larger p_T. Historically the Cronin effect was attributed to initial-state hard scattering [9,10], but this explanation remained unsatisfactory because it could not explain the much larger effect for protons compared to pions. Measurements of the momentum spectra at RHIC in the early 2000s renewed interest in the Cronin effect, and various theoretical models have been developed to explain it. Most models were based on hard and soft multiple scattering [11–15], but there were additional approaches involving gluon saturation [16] or hadronization by quark recombination [17]. To date, there is no full quantitative explanation of the Cronin effect.

There are striking similarities between long-range particle correlations in $A + A$ collisions and those observed in high multiplicity $p + p$ and $p + \mathrm{Pb}$ collisions at the Large Hadron Collider (LHC) [18–21]. This came as a surprise, because their presence in $A + A$ collisions was typically associated with the collective expansion of the QGP. Similar correlations were found in $d + \mathrm{Au}$ collisions at RHIC [22]. These findings have profound consequences for the interpretation of $p + \mathrm{A}$ collisions as a benchmark for cold-nuclear-matter effects and suggest that QGP could be produced in these systems. The PHENIX experiment has used the versatility of RHIC, which allows for collisions of light nuclei, such as p, d,

and ^{3}He, with larger nuclei, for systematic studies of particle correlations in small systems. In all systems studied, high multiplicity events show large azimuthal anisotropies, measured as v_2 and v_3, that can be related to the initial geometry of the collision system and the buildup of collective behavior of the produced particles [23–27], which would be indicative of QGP formation. This can also be seen at LHC energies where a measurement from $p + \mathrm{Pb}$ collisions [28] shows v_2 extending out past 20 GeV/c in p_T. These large azimuthal anisotropies also suggest the presence of radial flow in a hydrodynamic expansion, which would have an effect on the yield below a few GeV/c.

Results from long-range correlations have prompted great interest in finding other evidence of the possible formation of QGP in small systems, such as parton energy loss or thermal photon emission. In such studies, data sets are typically divided into "centrality classes" according to the particle multiplicity measured at forward rapidity on the side of the outgoing larger nucleus [29]. Indeed, in $p + \mathrm{Pb}$ collisions at the LHC [30] and $d + \mathrm{Au}$ collisions at RHIC [31], a suppression of the jet yield at high p_T was found for central collisions. However, the same analyses show a significant enhancement of the jet yield in peripheral collisions, putting in question if the observed suppression is due to energy loss [32] or whether there are other mechanisms at play, for example, x-dependent color fluctuation effects in protons [33,34] or biases in the centrality selection due to energy conservation [35].

In this paper, new data on the system size and centrality dependence of π^0 production are presented over a wide p_T range from 1 to 20 GeV/c from $p + \mathrm{Al}$, $p + \mathrm{Au}$, $d + \mathrm{Au}$, and $^3\mathrm{He} + \mathrm{Au}$ collisions at $\sqrt{s_{NN}} = 200$ GeV compared to $p + p$ collisions at the same energy. The data samples were recorded by the PHENIX experiment at RHIC during 2008 ($p + p$ 5.2 pb^{-1}, $d + \mathrm{Au}$ 80 nb^{-1}), 2014 ($^3\mathrm{He} + \mathrm{Au}$ 24 nb^{-1}), and 2015 ($p + p$ 60 pb^{-1}, $p + \mathrm{Al}$ 0.5 pb^{-1}, $p + \mathrm{Au}$ 0.2 pb^{-1}). The new $p + p$ data are combined with the published results from $p + p$ data taken in 2005 [36].

II. EXPERIMENTAL SETUP

To reconstruct the π^0 meson, the electromagnetic calorimeter (EMCal) in the central arms of the PHENIX detector is used. The EMCal is segmented into eight sectors, four in the west and four in the east arm of the PHENIX experiment. The sectors in each arm cover 90 deg in azimuth and ± 0.35 deg in pseudorapidity. All sectors in the west and the two top sectors in the east arm are made of 2 592 lead-scintillator (PbSc) towers each. The other two sectors use lead-glass crystals. For the analyses presented here, only the PbSc sectors were used. At a distance of 5 m from the nominal interaction point, the angular segmentation of the PbSc sectors

is $\Delta\phi \times \Delta\eta \approx 0.01 \times 0.01$. The energy resolution achieved is $\delta E/E \approx 2.1\% \oplus 8.3\%/\sqrt{E[\text{GeV}]}$ and arrival times of clusters are recorded with a resolution of $\approx$0.5 ns. Further details can be found in Ref. [37].

For event selection and for centrality characterization, the beam-beam counters (BBCs) are used, one on the north and one on the south side of the central arms. For asymmetric collision systems, the smaller (projectile) nucleus travels toward the north side and the larger (target) nucleus travels toward the south side. Each BBC is composed of 64 Čerenkov counter modules. The BBCs are located at ± 1.44 m from the interaction point and cover a pseudorapidity range of $3.0 < |\eta| < 3.9$. The BBC modules have a timing resolution of $\approx$0.1 ns.

While the EMCal and the BBC were identical for data collection in 2008, 2014, and 2015, there were new or modified detector components in each year. The most notable change was a silicon vertex tracker (VTX) installed in the central-arm acceptance in 2011. Although the VTX and other new components are not used in this analysis, the effect on the material budget needs to be taken into account in the GEANT3 [38] simulation used to calculate efficiency and acceptance corrections for each data set.

III. DATA SAMPLES

Several data samples were taken with different trigger conditions for each of the collision systems. The minimum-bias (MB) data samples require coincidental hits in each of the two BBCs. For the data recorded in 2014 and 2015, the event vertex was required to be within ± 10 cm of the nominal $z = 0$ position. For the data recorded in 2008, the requirement was ± 30 cm.

The collected MB data samples correspond to $\approx$88% of the inelastic cross section for $d + \text{Au}$ and $^3\text{He} + \text{Au}$, 84% for $p + \text{Au}$, 72% for $p + \text{Al}$, and 54% for $p + p$. The events that are not recorded by the MB trigger involve mostly single diffractive (SD) nucleon-nucleon collisions, which predominantly produce particles at forward or backward rapidity and thus do not lead to coincident hits in both BBCs. As the number of binary nucleon-nucleon collisions (N_{coll}) increases from $p + p$ to $^3\text{He} + \text{Au}$ collisions, the effect of an individual SD nucleon-nucleon collision is averaged out and a larger fraction of the inelastic cross section is captured by the MB trigger.

All MB data samples in the analysis, except for the $p + p$ samples, are subdivided into four centrality classes using the charge measured in the south BBC. The selections are 0–20%, 20–40%, 40–60%, and the remainder of the MB sample (>60%). Here the percentage refers to the fraction of events relative to all inelastic collisions.

The high luminosity provided by RHIC enables the increase of the statistics at high p_T, beyond what the data acquisition bandwidth would allow using an MB trigger only, by taking data samples with a high-energy threshold photon trigger, which PHENIX calls the ERT trigger. This trigger requires a minimum energy recorded in the EMCal segments (4×4 towers grouped to trigger tiles). Three different energy thresholds were used for each collision system. The ERT

TABLE I. ERT trigger thresholds (GeV) for each collision system.

	$p + p$	$p + \text{Al}$	$p + \text{Au}$	$d + \text{Au}$	$^3\text{He} + \text{Au}$
ERTA	2.1	2.8	2.8	2.8	3.5
ERTB	2.8	3.5	3.5	3.5	4.0
ERTC	1.4	2.1	2.1	2.1	2.8

trigger thresholds are summarized in Table I. No coincidence in the BBC was required. These samples are again divided into the same centrality classes as the MB sample.

During the $^3\text{He} + \text{Au}$, $p + \text{Au}$, and $p + \text{Al}$ data collection samples were also taken with a high multiplicity trigger. This trigger required, in addition to the BBC coincidence, a larger minimum charge in the south BBC, which corresponds to a larger number of fired BBC modules. The threshold was set to 25, 35, and 48 BBC modules, for $p + \text{Al}$, $p + \text{Au}$, and $^3\text{He} + \text{Au}$ respectively. The thresholds were chosen such that the data samples approximately correspond to the top 5% most central collisions for each system.

IV. DATA ANALYSIS

A. Yield measurement

Due to the high beam luminosity achieved at RHIC since 2010, PHENIX has recorded an increased number of double interactions that are largest for the $p + p$ data taken in 2015 and are noticeable for $p + \text{Au}$ and $p + \text{Al}$ data taken the same year. The effect is negligible for the $p + p$, $d + \text{Au}$, and $^3\text{He} + \text{Au}$ data taken in 2008 and 2014, respectively. For the 2015 data, double interactions were reduced by making cuts on the time of flight measured for towers in the EMCal and the BBC modules. The cut on the EMCal requires the tower time to be within ± 5 ns of the expected arrival time. This eliminates towers that are from different beam crossings. The BBC timing cut is used to reduce pile-up collisions that happen during the same bunch crossing. Such events are identified by large deviations of the time measured for individual BBC modules from the event average. For data from 2014 and 2008, no cuts were applied. Any residual pileup events are accounted for in the systematic uncertainties.

The reconstruction of neutral pions is performed via the $\pi^0 \to \gamma\gamma$ decay channel. The methods used by PHENIX have been described extensively in Ref. [39] and will only be summarized in this paper. As a first step, neighboring PbSc towers with energy deposits above 0.015 GeV are grouped into clusters. All clusters within one sector that have an energy of at least 0.3 GeV are combined into pairs. A minimum distance of 8 cm between the two cluster centers is required, corresponding to $\approx$1.5 tower separation between clusters. For each remaining pair, the invariant mass ($M_{\gamma\gamma}$) and p_T are calculated. Invariant-mass distributions are generated in bins of p_T and collision centrality. All mass distributions show a clear peak at the π^0 mass and a combinatorial background that is largest at events with low p_T and in central collisions.

To extract the π^0 yield, the background in the π^0 peak region needs to be subtracted. For p_T below 12 GeV/c, an asymmetry cut of $\alpha < 0.8$ is applied to reduce the
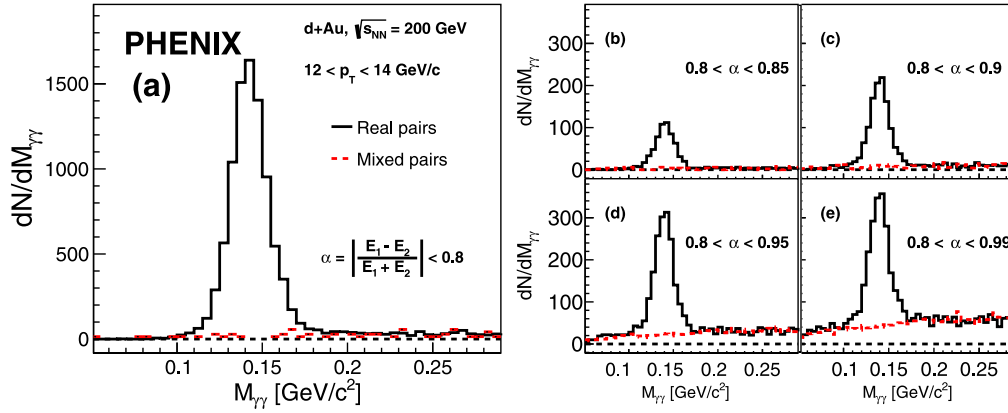
FIG. 1. (a) Invariant-mass example from d + Au collisions at $12 < p_T < 14\,\text{GeV}/c$. [(b)–(e)] The mass peak as a function of the asymmetry cut (α) on the two photons for the indicated α ranges.

combinatorial background. Here the asymmetry is defined as $\alpha = |\frac{(E_1 - E_2)}{(E_1 + E_2)}|$, where E_1 and E_2 are the energies of the two photon clusters. For p_T above $12\,\text{GeV}/c$, the cut is relaxed to $\alpha < 0.95$ as discussed below.

The bulk of the background is estimated and subtracted by an event mixing technique that combines clusters from different events with similar vertex position (z_vtx) and centrality. The shape of the mass distributions obtained from mixed events does not perfectly describe the combinatorial background in data. The mismatch results from correlated clusters in the event that are not accounted for in the mixed event technique.

For the MB samples, the mismatch is small and a two-step procedure is used for the subtraction. First, the mass distribution from mixed events is normalized in the mass region below and above the π^0 peak, $0.05 < M_{\gamma\gamma} < 0.1\,\text{GeV}/c^2$ and $0.2 < M_{\gamma\gamma} < 0.4\,\text{GeV}/c^2$, respectively. After subtracting the normalized distributions from all bins, a residual background remains. This is approximated by a line that is fitted to the same mass regions around the π^0 peak and then also subtracted.

For the ERT data samples, the shape difference is more significant and thus a different approach is used. Instead of normalizing the mixed event distribution with a constant, the ratio of data to mixed events is fit with a second-order polynomial in the window around the π^0 peak. This function is then used to normalize the mixed event distributions bin by bin, in the same mass intervals below and above the mass peak as in the MB samples (see above). No residual background subtraction is needed in this case.

At very high p_T, typically larger than $15\,\text{GeV}/c$, the combinatorial background is so small that neither normalization strategy for the mixed events gives stable results. Instead, the average count per mass bin, determined in the region below and above the π^0 peak, is subtracted.

After the background subtraction, yields of π^0 are calculated from the mass spectra by counting the entries within 2σ of the peak, where the σ is set by fitting the counts in the π^0 region to a Gaussian.

Above 12 GeV/c, the two photon clusters from the π^0 meson begin to overlap more and frequently merge into a single cluster. The asymmetry cut at $\alpha < 0.8$, which was used to reduce the combinatorial background, starts to limit the π^0 reconstruction efficiency and with it the effective p_T reach of the measurement. Because the combinatorial background is rather small at high p_T, the asymmetry cut can be relaxed to increase the reconstruction efficiency. Figures 1 and 2 show mass distributions from d + Au collisions in the $p_T = 12$ to $14\,\text{GeV}/c$ and 18 to $20\,\text{GeV}/c$ bins with different asymmetry cuts. The additional statistics recovered by extending the asymmetry cuts are clearly visible. In particular, in the higher p_T bin, increasing the cut from $\alpha < 0.8$ to <0.95 effectively increases the statistics. Because it is also evident that the background increases, the looser cut is only used above $p_T > 12$ GeV/c. The background subtraction and π^0 yield calculation follow the same steps as outlined above for lower p_T. The background estimate from event mixing is also shown on Fig. 1. In Fig. 2, the background is estimated from the average bin content around the π^0 peak.

B. Trigger selection

At this stage of the analysis, raw π^0 yields are available for all data samples in different bins of p_T and centrality. Figure 3(a) compares the raw yields from the MB and ERT samples in $p + p$ collisions from the 2015 data set. Figure 3(b) shows the ratio of individual samples to a common fit. The ERT trigger turn on curves are clearly visible.

In the next step, the raw yields from the MB and ERT trigger samples are combined for a given collision system and centrality. First, the ERT trigger samples are corrected for the trigger efficiency, which is calculated as a function of the π^0 p_T. The trigger efficiency has a smooth turn on around the trigger energy threshold and plateaus near 100% at higher p_T. A data-driven method is used that compares the ERTC to the MB sample and the ERTA/ERTB to the ERTC sample to establish the turn on curve of the different trigger thresholds. The corrected spectra agree very well in the range where the trigger efficiency is larger than 30%.

To assure the largest statistical accuracy in each p_T bin, the MB triggered events are used in the low-p_T region, the ERTC trigger in the mid-p_T region, and the ERTB trigger at
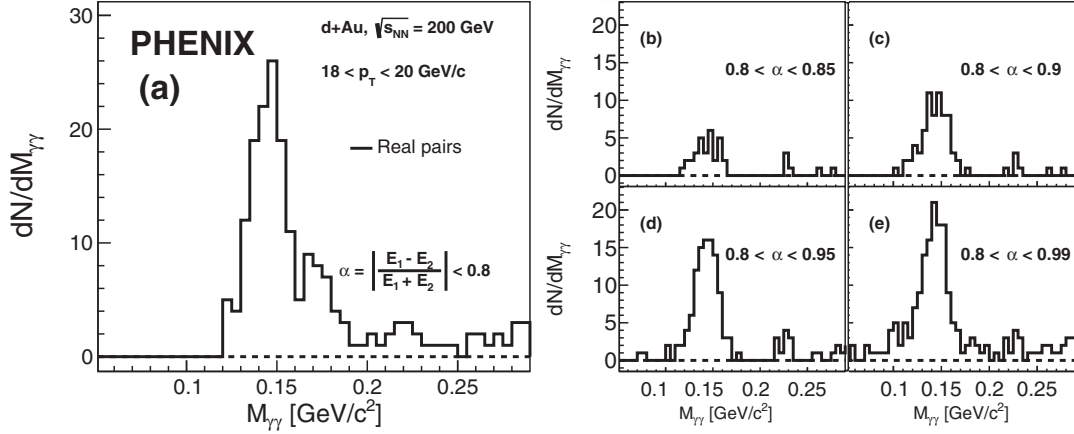
FIG. 2. (a) Invariant-mass example from $d + \mathrm{Au}$ collisions at $18 < p_T < 20\,\mathrm{GeV}/c$. [(b)–(e)] The mass peak as a function of the asymmetry cut (α) on the two photons for the indicated α ranges.

high p_T. These transitions happen at different p_T thresholds for different collision systems. The p_T thresholds are set near the point where the trigger efficiency reaches its plateau value, typically close to twice the trigger threshold shown in Table I. The ERTA triggered samples are used to cross check the results.

C. Corrections to the yield

Next, the raw p_T spectra need to be corrected for distortions due to the finite detector acceptance and overall detection efficiency (including detector effects and analysis cuts).

These are determined simultaneously as one single correction as a function of p_T using a full GEANT3 Monte Carlo (MC) simulation of the PHENIX detector setup. They are commonly referred to as acceptance-efficiency corrections (see Fig. 4), which are determined separately for each centrality selection to account for any multiplicity dependent effects. For each running period, a separate simulation setup is used that describes the PHENIX detector configuration specific to that period. Samples of single π^0 meson are simulated with a flat p_T distribution from 0 to 30 GeV/c, full azimuthal coverage, and in one unit of rapidity at midrapidity. The resulting simulated detector responses are embedded into real data from the same running period and reconstructed using the same analysis methods applied to the data. The simulation was tuned so that π^0 peak positions and widths reconstructed from the simulation matched the experimental data. Each reconstructed π^0 is weighted with a realistic production probability for the p_T of the input π^0. Because the true production probability is unknown, the weighting needs to be iterated. The probability is multiplied by the ratio of the measured raw π^0 distribution over the reconstructed π^0 distribution from the simulation.

FIG. 3. (a) Invariant yield example from 2015 $p + p$ collisions using different hardware trigger configurations. (b) The ratio of the different high-p_T triggers to a common Tsallis fit for all different triggers.
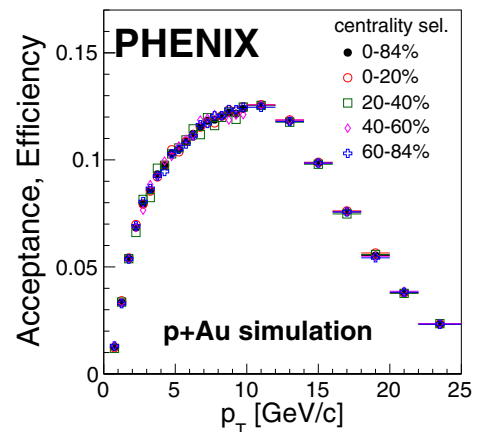

FIG. 4. The MC result of the acceptance and efficiency in $p + \mathrm{Au}$ collisions with the selected centrality classes as indicated.

TABLE II. Summary of the N_{coll}, N_{part}, N_{proj}, and f_{bias} calculated using a Glauber MC simulation [29,40]. The ratio N_{coll}/N_{proj} is also quoted for d and ^{3}He projectiles, because some systematic uncertainties cancel in this ratio. The last column is the measured charged particle multiplicity ($dN_{ch}/d\eta$) in the midrapidity region [40].

System	Centrality	$\langle N_{coll}\rangle$	$\langle N_{part}\rangle$	$\langle N_{proj}\rangle$	f_{bias}	$\langle N_{coll}\rangle/\langle N_{proj}\rangle$	$dN_{ch}/d\eta$
$p+p$		1	2	1	0.73 ± 0.07		2.38 ± 0.09
$p+$Al	0–5%	4.1 ± 0.3	4.5 ± 0.3	1	0.81 ± 0.01		5.5 ± 0.8
	0–20%	3.4 ± 0.3	4.4 ± 0.3	1	0.81 ± 0.01		5.1 ± 0.7
	20–40%	2.3 ± 0.1	3.3 ± 0.1	1	0.90 ± 0.02		4.0 ± 0.6
	40–60%	1.8 ± 0.1	2.8 ± 0.2	1	0.99 ± 0.03		3.3 ± 0.3
	60–72%	1.3 ± 0.1	2.3 ± 0.2	1	1.15 ± 0.06		2.7 ± 0.1
	0–100%	2.1 ± 0.1	3.1 ± 0.1	1	0.80 ± 0.02		4.0 ± 0.5
$p+$Au	0–5%	9.7 ± 0.6	10.7 ± 0.6	1	0.86 ± 0.01		12.3 ± 1.7
	0–20%	8.2 ± 0.5	9.2 ± 0.5	1	0.90 ± 0.01		10.4 ± 1.5
	20–40%	6.1 ± 0.4	7.1 ± 0.4	1	0.98 ± 0.01		7.7 ± 1.1
	40–60%	4.4 ± 0.3	5.4 ± 0.3	1	1.02 ± 0.01		5.7 ± 0.8
	60–84%	2.6 ± 0.2	3.6 ± 0.2	1	1.00 ± 0.06		3.5 ± 0.5
	0–100%	4.7 ± 0.3	5.7 ± 0.3	1	0.858 ± 0.014		6.7 ± 0.9
$d+$Au	0–5%	18.1 ± 1.2	17.8 ± 1.2	1.97 ± 0.02	0.91 ± 0.01	8.98 ± 0.59	18.9 ± 1.4
	0–20%	15.1 ± 1.0	15.2 ± 0.6	1.95 ± 0.01	0.94 ± 0.01	7.46 ± 0.50	16.4 ± 1.2
	20–40%	10.2 ± 0.7	11.1 ± 0.6	1.84 ± 0.01	1.00 ± 0.01	5.71 ± 0.39	12.2 ± 0.9
	40–60%	6.6 ± 0.4	7.8 ± 0.4	1.65 ± 0.02	1.03 ± 0.02	4.16 ± 0.28	8.7 ± 0.6
	60–88%	3.2 ± 0.2	4.3 ± 0.2	1.36 ± 0.02	1.03 ± 0.06	2.27 ± 0.15	4.1 ± 0.3
	0–100%	7.6 ± 0.4	8.6 ± 0.4	1.62 ± 0.01	0.889 ± 0.003	4.35 ± 0.24	9.5 ± 1.0
^{3}He $+$ Au	0–5%	26.1 ± 2.0	25.0 ± 1.6	2.99 ± 0.01	0.92 ± 0.01	8.72 ± 0.64	23.6 ± 2.6
	0–20%	22.3 ± 1.7	21.8 ± 1.3	2.95 ± 0.01	0.95 ± 0.01	7.30 ± 0.52	21.4 ± 2.3
	20–40%	14.8 ± 1.1	15.4 ± 0.9	2.75 ± 0.03	1.01 ± 0.01	5.41 ± 0.37	16.1 ± 1.8
	40–60%	8.4 ± 0.6	9.5 ± 0.6	2.29 ± 0.04	1.02 ± 0.01	3.85 ± 0.25	10.3 ± 1.1
	60–88%	3.4 ± 0.3	4.6 ± 0.3	1.56 ± 0.05	1.03 ± 0.05	2.05 ± 0.12	4.4 ± 0.5
	0–100%	10.4 ± 0.7	11.4 ± 0.5	2.22 ± 0.02	0.89 ± 0.01	4.13 ± 0.24	12.2 ± 1.4

The modified probability is then used as the new weight. The process is iterated until convergence, which typically requires only a few steps. The final acceptance-efficiency corrections are calculated as the ratio of the reconstructed number of π^0 at a given p_T over the number of generated ones at that p_T in one unit of pseudorapidity at midrapidity and 2π in azimuth.

Additionally, the yield in each centrality selection for a given collision system must be corrected for the bias toward higher event multiplicity, and hence more central events, for nondiffractive nucleon-nucleon collisions compared to diffractive collision events with the same impact parameter (see Ref. [29] for full details). The bias factor f_{bias}, which is used to scale the p_T spectra, is calculated using a Glauber model MC calculation [41] in conjunction with the assumption of a negative-binomial multiplicity distribution of particles produced in individual nucleon-nucleon collisions. The same Glauber calculation is used to characterize each centrality class by the number of binary nucleon-nucleon collisions N_{coll}, number of nucleon participants N_{part}, and other relevant properties related to the collision geometry, such as N_{proj}, the number of participants in the projectile nucleus. For MB collisions, the f_{bias} also includes the extrapolation from the recorded cross section to the full inelastic cross section (0–100% centrality). The average values of N_{coll}, N_{part}, N_{proj}, and the bias factor f_{bias} are given in Table II.

V. SYSTEMATIC UNCERTAINTY

There are many sources of systematic uncertainty that need to be evaluated. They are separated into two groups: (i) uncertainty on the event characterization and (ii) uncertainty on the π^0 yield extraction.

The event characterization is done using Glauber model simulations and the uncertainties were determined by varying the input to the Glauber model and various assumptions used in Ref. [29]. The results are included in Table II. The quantities calculated from the Glauber model simulation are highly correlated. For example, any change in the assumed nucleon-nucleon cross section will lead to a simultaneous change of N_{coll}, N_{part}, and N_{proj}. Thus, in ratios such as N_{coll}/N_{proj}, some of the systematic uncertainties cancel. This was taken into account in the errors quoted in Table III.

The uncertainties on the π^0 invariant yield are summarized in Table III for the different running periods. The total uncertainty on the π^0 invariant yield varies between 8 and 10% for p_T below 8 GeV/c and increases to nearly 15% at 20 GeV/c. They have little dependence on collision systems or centrality selection. The uncertainties on the π^0 invariant yield were obtained with similar methods for all data sets. They are highly correlated within a running period and somewhat correlated between running periods. In particular, the uncertainty on the energy scale and the uncertainty due to shower merging are correlated between all data sets. In 2014

TABLE III. Summary of systematic uncertainties on the π^0 invariant yields from different running periods.

Systematic uncer. p_T [GeV/c]	2015 p + Au, p + Al, p + p			2014 ^{3}He + Au			2008 d + Au, p + p		
	2	8	20	2	8	20	2	8	20
Peak extraction	4.4%	3.4%	1%	2.7%	4.1%	2%	4.8%	2.9%	1.5%
Energy scale	3.8%	6.5%	7.1%	3.0%	5.2%	5.7%	4.6%	7.9%	8.7%
Acceptance-efficiency	3%	2.5%	1%	4%	4%	4%	3%	2.5%	1%
Cluster merging	<0.1%	<0.1%	9.0%	<0.1%	<0.1%	12%	<0.1%	<0.1%	10%
Conversion loss	5%	5%	5%	5%	5%	5%	2.5%	2.5%	2.5%
Double interactions	4%	3%	4%	<1%	<1%	<1%	1%	2.5%	4%
Off-vertex decays	3%	3%	3%	3%	3%	3%	3%	3%	3%
Total	9.6%	10.1%	13.0%	8.3%	9.8%	14.1%	8.3%	10.0%	14.5%

and 2015, the experimental setup was nearly identical and therefore the acceptance-efficiency correction, losses due to photon conversions, and uncertainties due to off-vertex decays are also correlated for data sets taken during those years. For data sets taken within the same running period, all systematic uncertainties, except for the π^0 peak extraction and the effect of double interactions, are correlated. The correlations of the systematic uncertainties have been taken into account when combining data sets or calculating ratios of data sets by determining the full error matrix and using the Best Linear Unbiased Estimate (BLUE) algorithm [42–44] to calculate the weight for each p_T and each measurement.

The remainder of this section provides more details on the evaluation of the systematic uncertainties on the π^0 yield determination, which is split into the extraction of the raw π^0 yield and the corrections that need to be applied to it.

A. Raw π^0 yield extraction

The raw π^0 yield is extracted from an invariant mass $M_{\gamma\gamma}$ distribution, which involves the subtraction of a background distribution below a π^0 peak. Except for at very high p_T, this is done using the mixed event technique. This subtraction is typically accurate to better than 4%. In general, the uncertainties on the background subtraction are determined by changing the assumption on the shape of the background and how it is normalized. Many different strategies can be used, as they all give similar results. Here, one example is given, the strategy that was used for the 2015 MB data sets, which were used to extract the π^0 yield at lower p_T values for p + Au, p + Al, and p + p. The normalization of the mixed event background is determined in different ranges below and above the π^0 peak. For any normalization, after the mixed event subtraction there is a residual background, which is then fitted. For each normalization the fit range is varied to extract the residual background via a first-order polynomial. Then in each case the window for the π^0 yield extraction is varied from 1 to 3 sigma around the π^0 peak. The variation of the resulting π^0 yields, after correcting for the different σ ranges, is used to estimate the systematic uncertainty.

The accuracy with which the π^0 yield can be extracted depends on the amount of background. In general, the smaller the particle multiplicity in the event and/or the larger the π^0 p_T, the smaller the background. However, the accuracy with

which the background can be determined for a particular p_T and centrality bin is driven by the available statistics. The dominant effect changes depending on the π^0 p_T and the MB or ERT data set.

B. Corrections of the raw yield

The acceptance-efficiency correction accounts for all distortions to the π^0 spectra that can be evaluated with the detailed simulation of π^0 measurements in the PHENIX experiment. The accuracy of the simulation determines the size of systematic uncertainties. Accordingly, the simulation output was carefully compared to the data.

These distortions include, besides the actual corrections for detector acceptance and π^0 reconstruction, the one for the energy scale and resolution, merging of clusters, and losses due to photon conversions. While the corrections were determined simultaneously, possible uncertainties are studied separately. In Table III, these are identified as "acceptance-efficiency," "energy scale," "cluster merging," and "conversion loss," respectively.

The energy scale and resolution was tuned by matching the π^0 peak position and width in simulation and data, as function of p_T, to a better than 0.5–1% agreement, depending on the data set. The uncertainty is then determined by varying the energy scale and resolution within the achieved accuracy. The π^0 yields change by less than 4–5% at 2 GeV/c and up to 7–9% at 20 GeV/c.

To study the accuracy of the reconstruction efficiency correction, cuts applied in the π^0 reconstruction were varied and the analysis was repeated. The changes in the π^0 yield were used to set the systematic uncertainties. They are typically smaller than 4%, but may be limited by statistical uncertainties. The uncertainty on the acceptance was determined from the precision of the survey of the EMCal. It is negligible compared to the uncertainties on the reconstruction efficiency.

Because the two decay photons from the decay of a high p_T π^0 are strongly boosted along the π^0 direction, the average opening angle becomes small, resulting in only a small separation between the impact points on the surface of the EMCal. At $\approx$10 GeV/c, the two clusters start to merge. Initially, this happens only for very symmetric decays characterized by a small energy asymmetry (α). With increasing p_T, more clusters merge, leading to an systematic decrease in reconstruction

efficiency toward higher p_T. The accuracy with which the MC simulation reproduces the cluster merging is verified by reconstructing π^0 mesons from three exclusive asymmetry bins: 0–0.4, 0.4–0.8, and 0.8–0.95. After fully correcting the π^0 yields, the results are compared and the differences are used to estimate the systematic uncertainty. It reaches $\approx 10\%$ toward the end of the kinematic reach of the measurement.

Some photons convert into e^+e^- pairs before they reach the EMCal. If the radial location of the conversion point is close to the EMCal, outside the magnetic field, the e^+ and e^- will hit the EMCal in close proximity, resulting in one cluster with the full energy of the converted photon. In that case, it is likely that the π^0 is reconstructed. However, if the conversion point is closer to the vertex, and in the magnetic field, the π^0 will not be reconstructed, because the electron tracks bend in opposite directions, depositing their energy in two separate clusters.

Prior to 2010, before the VTX was installed, $\approx 10\%$ of the π^0 were not reconstructed because one of the photons converted in the detector material. Due to the additional material of the VTX detector close to the vertex, this number increases to $\approx 24\%$. The accuracy with which the loss can be determined depends solely on the accuracy with which the material budget is known and implemented in the GEANT3 simulation. The resulting uncertainties on the π^0 yield are 2.5% and 5%, before and after installation of the VTX. There is no significant momentum dependence.

All data sets from 2015 ($p + p$, $p + $Al, and $p + $Au) were taken at high instantaneous luminosity, resulting in a significant number of recorded double interactions. These were actively identified and removed by timing cuts on the EMCal and BBC. The effect of any remnant double interaction was estimated by splitting the data samples into subsets taken at higher, medium, and lower luminosity. The analysis was repeated for each sample, and the π^0 yields were found to be consistent within 3–4%. This difference was assigned as a systematic uncertainty. For the 2008 data sets ($p + p$ and $d + $Au), only the EMCal timing cuts were applied to remove pileup events. Here, the possible contamination was estimated by the number of π^0 for which at least one cluster had a time off by >5 ns. The contribution was 1% at high p_T and $\approx 4\%$ at lower p_T. For the 2014 ^{3}He $+$ Au data, no sizable effect was found.

Finally, the uncertainty of the normalization of the data taken with the ERT trigger to the MB data is examined. It is estimated from the uncertainty on the linear fit of the ratio between the ERT and MB data in the region where the ERT trigger is fully efficient. This uncertainty is smaller than 1% and not listed in Table III.

VI. RESULTS AND DISCUSSION

A. The $p + p$ reference

PHENIX has previously published the π^0 p_T spectrum from $p + p$ collisions at $\sqrt{s} = 200$ GeV [36] based on data taken in 2005 corresponding to 3.4 pb^{-1}. In 2008 and 2015, RHIC provided further $p + p$ collisions, increasing the integrated luminosity by 5.2 and 60 pb^{-1} respectively.
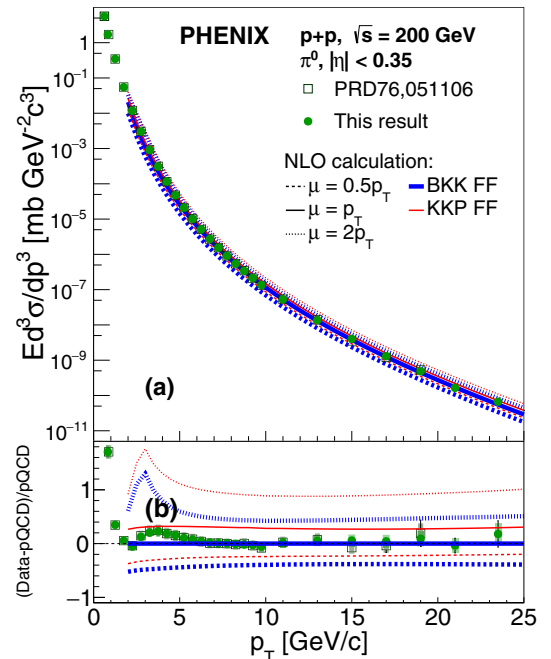

FIG. 5. (a) Differential cross section of π^0 in $p + p$ collisions at $\sqrt{s} = 200$ GeV. The data are compared with the indicated pQCD calculations. (b) The ratio of the data points to the NLO calculation with BKK and a scale of $\mu = p_T$.

With the increase in the data sample, the precision of the measurement was improved and extended to higher p_T. Because the detector configurations and the ERT trigger settings were different for the 2008 and 2015 data sets, the π^0 spectra were measured separately. The results were combined with those from 2005.

The new and published measurements were made with the PHENIX EMCal using the same analysis strategy, and thus the π^0 yield determinations have largely, but not completely, correlated systematic uncertainties. To combine the three data sets, the correlations between individual systematic uncertainties were studied and accounted for using the BLUE method [43]. In addition to the uncertainties due to the π^0 reconstruction, there is an overall normalization uncertainty of 9.7% [36] that accounts for the limited accuracy with which the $p + p$ MB trigger efficiency (see Table II) is known. This uncertainty is common to all $p + p$ measurements.

Figure 5 compares the combined π^0 p_T spectrum from $p + p$ collisions (2005, 2008, 2015) to the earlier published result. The combined result is in excellent agreement with data taken in 2005, but has significantly improved statistics and extends the p_T range up to 25 GeV/c. The systematic uncertainties are slightly reduced with respect to those of the 2005 data alone.

Also shown in Fig. 5 are next-to-leading-order (NLO) perturbative-quantum-chromodynamics (pQCD) calculations [45] with two different fragmentation functions (BKK and KKP) and for three different scales $\mu = p_T/2$, p_T, and $2p_T$. For the calculations, the same CT14 free proton parton distribution function (PDF) was used and only the fragmentation function in the same framework was changed. Within the assumed range of scales, both fragmentation functions are
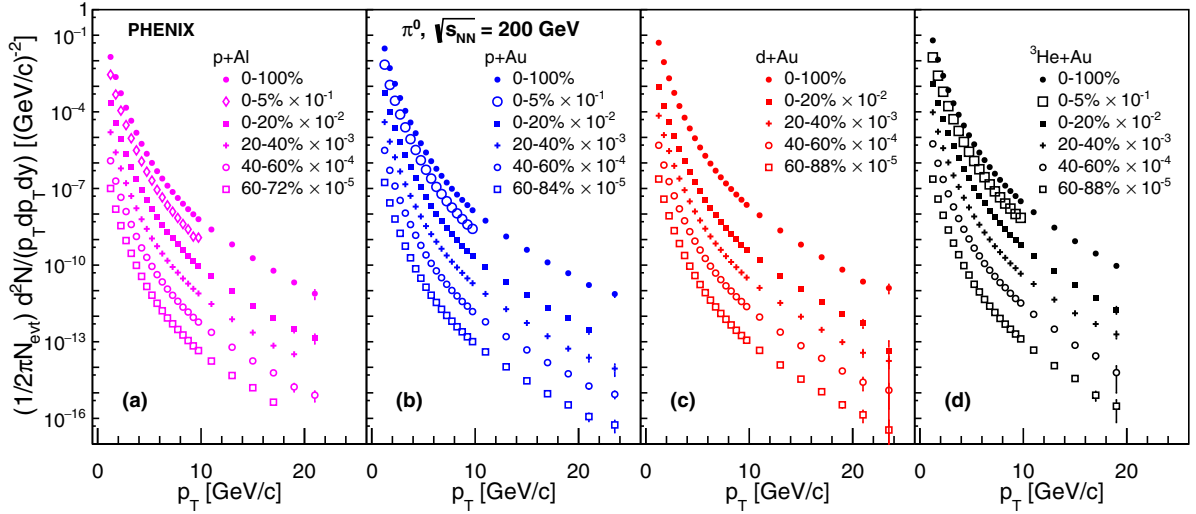
FIG. 6. Invariant yield of π^0 from (a) $p + $ Al, (b) $p + $ Au, (c) $d + $ Au, and (d) ^{3}He $+ $ Au at $\sqrt{s_{NN}} = 200$ GeV. For each collision system the yield is shown for the inelastic cross section and for different centrality selections 0–20%, 20–40%, 40–60%, and larger than 60%. For $p + $ Al, $p + $ Au, and ^{3}He $+ $ Au an additional 0–5% centrality selection is shown, which was recorded using a dedicated high multiplicity trigger.

consistent with the data. BKK would require a scale of $\mu = p_T$, while KKP envelopes the data between $\mu = p_T/2$ and p_T scales.

B. Small system p_T spectra and nuclear-modification factor

To simplify the labeling and description of each variable, the same notation is used for each small system. The "projectile" nucleus (p, d, or ^{3}He) is denoted by x and the "target" nucleus (Au or Al) is indicated by A. This notation is used in both the plots and text unless a specific system is being discussed.

1. p_T spectra

Figure 6 presents π^0 p_T spectra from (a) $p + $ Al, (b) $p + $ Au, (c) $d + $ Au, and (d) ^{3}He $+ $ Au. The data are presented as the invariant π^0 yield per collision as a function of p_T. The 0–100% range corresponds to the full inelastic cross section. The other centrality ranges correspond to 0–5%, 0–20%, 20–40%, 40–60%, and above 60% measured percentile of the events selected according to the multiplicity measured in the BBC on the south side (heavy nucleus going side). Different centrality selections are scaled by factors 1/10 for visibility. The 0–5% centrality selection, which is available for ^{3}He $+ $ Au, $p + $ Au, and $p + $ Al collisions, was taken with a high multiplicity BBC trigger and has a p_T range limited to below 10 GeV/c.

2. Nuclear-modification factor

For a quantitative comparison across systems and centrality selections the nuclear-modification factor (R_{xA}) is used. It is defined as

$$R_{xA} = \frac{dN_{xA}/dp_T \times \sigma_{pp}^{\text{inel}}}{\langle N_{\text{coll}} \rangle \times d\sigma_{pp}/dp_T},$$ (1)

where dN_{xA}/dp_T is the invariant yield per $x+$A collisions, $d\sigma_{pp}/dp_T$ is the invariant cross section in $p + p$ collisions, $\sigma_{pp}^{\text{inel}} = 42$mb is the inelastic $p + p$ cross section, and $\langle N_{\text{coll}} \rangle$ is the average number of binary nucleon-nucleon collisions given in Table II. The $\langle N_{\text{coll}} \rangle$ is obtained by the Glauber MC model [46] used in all PHENIX papers and the detailed study of the model in smaller system centrality applications was described in Ref. [29]. A nuclear-modification factor of $R_{xA} \approx 1$ at high p_T indicates that π^0 production through hard scattering processes in $x + A$ collisions is well described by an incoherent superposition of $p + p$ collisions.

3. R_{xA} for inelastic collisions

The nuclear-modification factors, R_{xA}, for inclusive π^0 production from inelastic $p + $ Al, $p + $ Au, $d + $ Au, and ^{3}He $+ $ Au collisions are shown in Fig. 7. They are calculated using the $p + p$ reference from the combined 2005, 2008, and 2015 data. The correlations of the systematic uncertainties on the π^0 reconstruction for different data sets are taken into account using the BLUE method. The overall normalization uncertainties on $p + p$ and on N_{coll} are shown separately at the lowest and highest p_T, respectively.

Each data set exhibits the characteristic p_T dependence of the Cronin effect, an initial rise from below unity to a peak around p_T of 4 GeV/c, followed by a drop and a leveling off at high p_T. The constant value at high p_T is independent of the collision system at a value of $R_{xA} \approx 0.9$, which is consistent with unity within the systematic uncertainties on the scale and N_{coll}. The fact that R_{xA} at high p_T is consistent with unity and that there is no system size dependence suggests that there is little to no modification of the hard scattering component in small systems.

To investigate any possible system size dependence of the modification at lower p_T, the ratio of the maximum of R_{xA} divided by the integral taken above 10 GeV/c. This corresponds to the height of the peak in R_{xA} assuming that R_{xA} at high
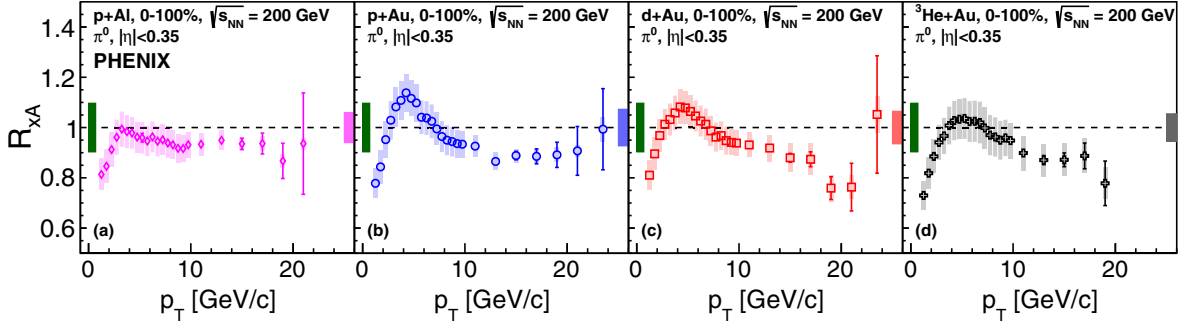
FIG. 7. Nuclear-modification factors from inelastic (a) $p + \text{Al}$, (b) $p + \text{Au}$, (c) $d + \text{Au}$, and (d) $^3\text{He} + \text{Au}$ collisions at $\sqrt{s_{NN}} = 200\,\text{GeV}$. The error bars represent the statistical uncertainties, while the boxes represent the systematic uncertainties. The high-p_T box in each panel is the N_{coll} uncertainty from the Glauber model, while the low-p_T box represents the overall normalization uncertainty from $p + p$ collisions.

p_T is indeed unity. In these ratios the systematic uncertainties largely cancel. The values are 1.06 ± 0.09, 1.25 ± 0.11, 1.17 ± 0.10, and 1.17 ± 0.12 for $p + \text{Al}$, $p + \text{Au}$, $d + \text{Au}$, and $^3\text{He} + \text{Au}$, respectively. The value is smallest in $p + \text{Al}$ collisions and most pronounced in $p + \text{Au}$ collisions. In addition, the maximum in R_{xA} moves toward higher p_T with increasing system size from $3.25\,\text{GeV}/c$ in $p + \text{Al}$ to $4.25\,\text{GeV}/c$ in $p + \text{Au}$ and $d + \text{Au}$ to $5.25\,\text{GeV}/c$ in $^3\text{He} + \text{Au}$.

The values are approximately the same as the peak heights calculated in fixed target $p + A$ experiments [47] and as originally predicted for RHIC energies [11,14,15]. However, the systematic trend with system size does not follow the dependence observed at fixed target energies [8],

$$\frac{d\sigma_{xA}}{dp_T} = (xA)^{n(p_T)} \times \frac{d\sigma_{pp}}{dp_T}, \qquad (2)$$

with a common exponent $n(p_T)$ for a given $\sqrt{s}$. Here, xA stands for the product of the number of nucleons in the small and large ions. Equation (2) is rewritten in terms of per event yield by factoring out the inelastic cross sections $\sigma_{xA}^{\text{inel}}$ and $\sigma_{pp}^{\text{inel}}$:

$$\frac{dN_{xA}}{dp_T} = (xA)^{n(p_T)} \times \frac{\sigma_{pp}^{\text{inel}}}{\sigma_{xA}^{\text{inel}}} \times \frac{dN_{pp}}{dp_T}. \qquad (3)$$

In the case of no nuclear modification for hard scattering processes, the per event yields in $x + A$ and $p + p$ collisions are related through the number of binary nucleon-nucleon collisions N_{coll}. In this case, the exponent $n(p_T) = 1$ and N_{coll} is

$$\langle N_{\text{coll}} \rangle = xA \times \frac{\sigma_{pp}^{\text{inel}}}{\sigma_{xA}^{\text{inel}}}. \qquad (4)$$

This identity can be used to relate the nuclear-modification factor, R_{xA}, and the exponent $n(p_T)$:

$$n(p_T) = 1 + \frac{\log(R_{xA})}{\log(xA)}. \qquad (5)$$

The exponent $n(p_T)$ is calculated from the ratio of $R_{p\text{Au}}/R_{p\text{Al}}$ and $R_{\text{HeAu}}/R_{p\text{Au}}$. The uncertainties due to the $p + p$ cross section cancel in the ratios; so do most of the uncertainties on the N_{coll} calculation. The results are shown in Fig. 8. The data show that there is no universal $n(p_T)$ at

$\sqrt{s_{NN}} = 200\,\text{GeV}$ below 8–10 GeV/c. At higher p_T, the common $n(p_T)$ underlines the similarity of R_{xA} for all collision systems.

4. R_{xA} centrality dependence

In Fig. 9, R_{xA} is shown for the different centrality selections from different collision systems. The scale uncertainty from the $p + p$ reference and, to a large extent, the scale uncertainty due to N_{coll} only influences the scale of R_{xA}, but not the relative differences between systems. The comparison reveals clear systematic trends of R_{xA} with centrality and system size.

For $p_T > 8\,\text{GeV}/c$, the R_{xA} values remain constant at similar values for the same centrality selection from different collision systems. However, the plateau value varies with centrality. R_{xA} is below unity in the more central collisions, consistent with unity in the 20–40% bin, and above or consistent with unity in the peripheral collisions. In the lower p_T range, the 0–5% and 0–20% selections exhibit a clear Cronin peak structure, similar to the 0–100% case, but more pronounced. The height of the peak is largest for $p + \text{Au}$. The height of the peak is system size dependent and decreases
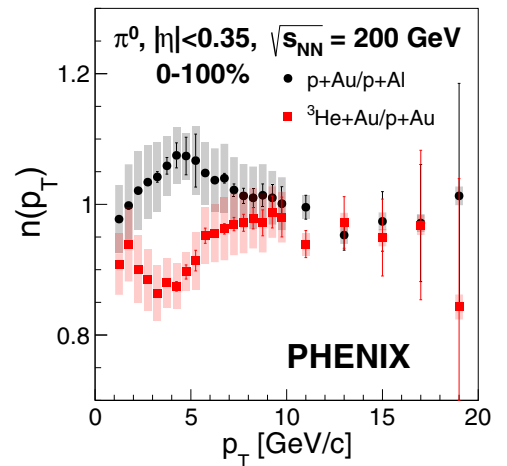

FIG. 8. Exponent according to Eq. (5) as a function of transverse momenta extracted from $p + \text{Au}/p + \text{Al}$ and $^3\text{He} + \text{Au}/p + \text{Au}$ collision systems. The uncertainties from the N_{coll} calculations and from the overall normalization of $p + p$ cancel in these ratios.
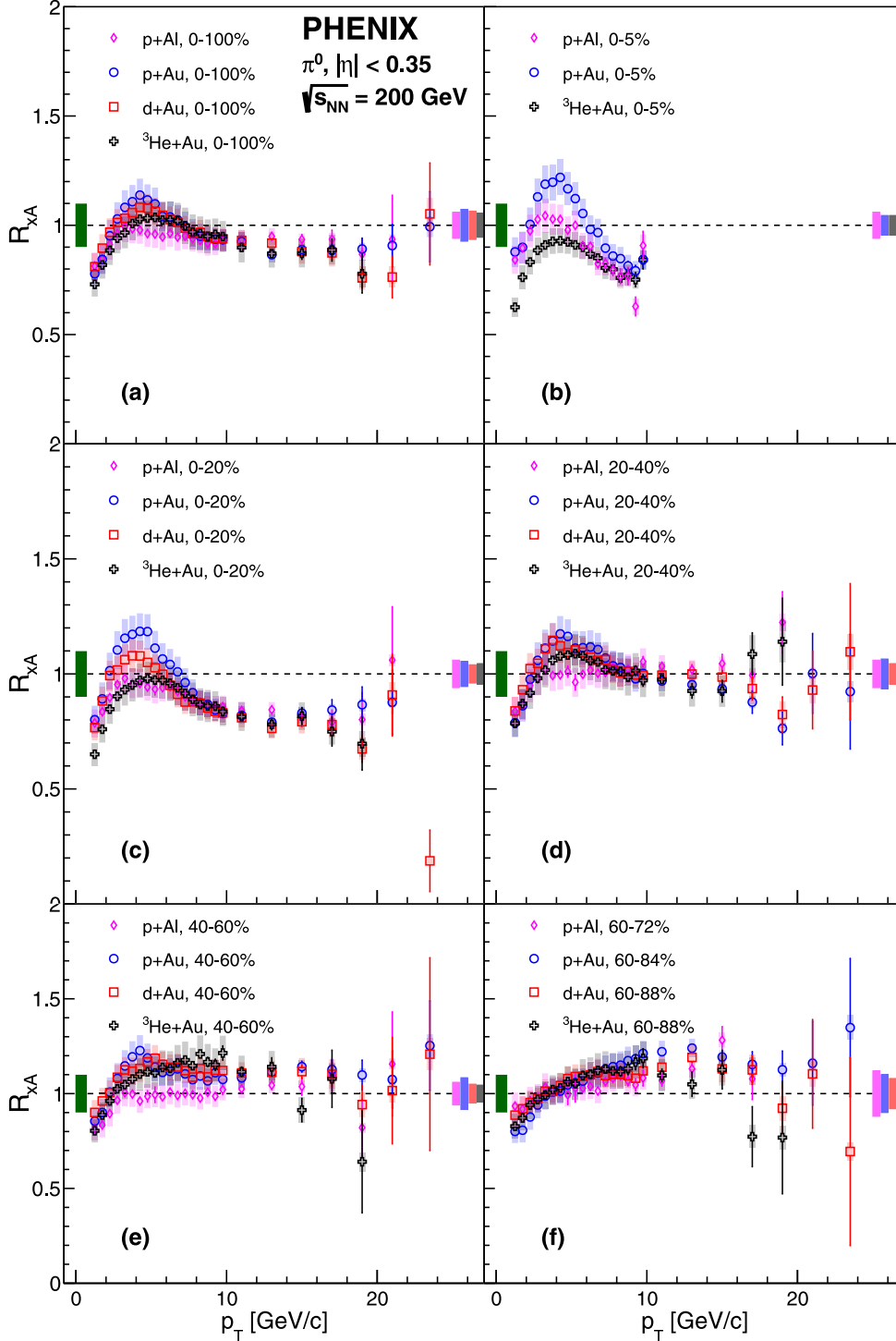
FIG. 9. Nuclear-modification factors in $p + $ Al, $p + $ Au, $d + $ Au, and ^{3}He $+$ Au in 0–100% and the five indicated centrality bins and for inelastic collisions at $\sqrt{s_{NN}} = 200$ GeV. The error bars represent the statistical uncertainties, while the boxes represent the systematic uncertainties. The high-p_T boxes are the uncertainties of the N_{coll} collisions from the Glauber model, while the low-p_T box represents the overall normalization uncertainty from $p + p$ collisions.

from $p + $ Au, to $d + $ Au, to ^{3}He $+$ Au, i.e., with increasing size of the projectile nucleus. The peak is smaller for $p + $ Al than for $p + $ Au, so it also seems to decrease with decreasing size of the target nucleus. In contrast, in peripheral collisions all systems follow a common trend. Though there is a gradual

change between central and semiperipheral collisions, it is not consistent between systems.

To better understand the trends, the average nuclear-modification factor $\langle R_{xA} \rangle$ is calculated for two distinct p_T regions, above 8 GeV/c to represent the high p_T region and
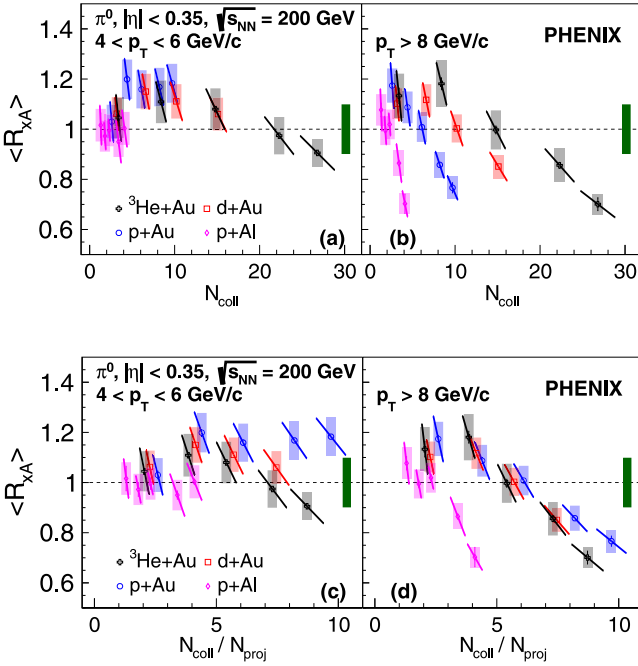
FIG. 10. Average R_{xA} vs the number of collisions for (a) the region around the R_{xA} peak [$4 < p_T < 6$ GeV/c] and (b) the high-p_T region [$p_T > 8$ GeV/c]. [(c), (d)] Average R_{xA} vs the number of collisions per projectile participant for the same two p_T ranges. The statistical (error bars) and systematic (boxes) uncertainties are indicated. The tilted error bars represent the anticorrelated uncertainty on the y and x axes due to the N_{coll} calculations. The bar around unity at the highest p_T shown represents the overall normalization uncertainty from $p + p$ collisions.

from $4 < p_T < 6$ GeV/c to capture the peak of R_{xA}. These $\langle R_{xA} \rangle$ are studied as function of N_{coll} and N_{coll}/N_{proj} shown in Table II. Hard scattering processes are expected to scale with N_{coll}, and thus N_{coll} is a natural choice. If the nucleons in the projectile interact independently with the target nucleus, nuclear modifications should not depend on N_{coll}, but rather N_{coll}/N_{proj}. Note that N_{coll} and N_{part} are highly correlated and follow a common trend. In peripheral collisions, nucleons in the projectile are generally striking unique nucleons in the target and $N_{part} = N_{coll} + 1$ up to an N_{coll} value of ≈ 14. For $N_{coll} > 14$, N_{part} increases slightly slower with N_{coll} as nucleons start to participate in multiple interactions. Consequently, common trends of a nuclear modification with N_{coll} will also present themselves with respect to N_{part}. The $\langle R_{xA} \rangle$ is calculated as follows:

$$\langle R_{xA} \rangle = \frac{\int \frac{dN_{xA}}{dp_T} dp_T}{N_{coll} \int \frac{dN_{pp}}{dp_T} dp_T}. \quad (6)$$

Figure 10 shows $\langle R_{xA} \rangle$ for the two p_T regions for all measured centrality selections from all collision systems. In Figs. 10(a) and 10(b) $\langle R_{xA} \rangle$ is plotted as function of N_{coll} and in Figs. 10(c) and 10(d) as function of N_{coll} per number of participating nucleons in the projectile N_{proj}.

Figure 10(a) shows $\langle R_{xA} \rangle$ as function of N_{coll} for the lower p_T range from 4 to 6 GeV/c, covering the peak in R_{xA} for all systems. The $\langle R_{xA} \rangle$ is remarkably close to binary scaling, with

deviations that are visibly smaller than those observed at high p_T [see Fig. 10(b)]. Another notable difference compared to the high-p_T range is that all systems show similar deviations from binary scaling at the same N_{coll}. In contrast, the systems involving a Au target nucleus do not show a common trend with N_{coll}/N_{proj} [see Fig. 10(c)]. These observations are qualitatively the same for any p_T window between 1 and 6 GeV/c, which suggests that the mechanism underlying the nuclear modification is different at high and low p_T with a transition in the 5 to 7 GeV/c range.

Figure 10(b) shows that for p_T above 8 GeV/c the $\langle R_{xA} \rangle$ exhibits no common trend as function of N_{coll}. The $\langle R_{xA} \rangle$ is below N_{coll} scaling for central classes and above for peripheral classes for all collision systems. The situation changes when looking $\langle R_{xA} \rangle$ versus N_{coll}/N_{proj} [see Fig. 10(d)]. The collision systems involving Au as a target nucleus ($p + $Au, $d + $Au, and ^{3}He $+ $Au) follow a common trend. For Al as a target nucleus, a distinctly different trend is observed. The modifications to binary scaling or $\langle R_{xA} \rangle$ remain approximately the same for similar $p + $Au and $p + $Al centrality classes, but occur at different N_{coll}/N_{proj}. The same trends are observed for any choice of p_T threshold above 7 up to 15 GeV/c, above which the statistical precision is limited. There are two model-independent conclusions that can be derived from the observations: (i) The underlying mechanism for the nuclear modification does not depend on the projectile nucleus and (ii) the nuclear modification is not driven by the thickness of the nuclear matter traversed by the projectile.

5. Model comparison and discussion

The PDF of a nucleon is modified if the nucleon is within a nucleus and the modifications increase with increasing number of nucleons in the nucleus. Similarly to the free proton PDFs themselves, the nuclear parton distribution functions (nPDFs) are determined empirically by fitting a large variety of experimental data. Here three different nPDFs are considered: nNNPDFv1.0 [48], EPPS16 [49], and nCTEQ15 [50]. For consistency, the same framework was used in all calculations with the same fragmentation function [51].

Figure 11 compares the measured nuclear-modification factors for inclusive $p + $Al, $p + $Au, $d + $Au, and ^{3}He $+ $Au collisions to the predictions using the three different nPDFs mentioned above. The central value of the predictions is represented by a line and the uncertainties from fitting the nPDF to data are given as shaded area. Due to their large uncertainties, all three nPDFs give R_{xA} predictions consistent with the data. However, looking at the central values, the predictions are in tension with the trends of the data. For example, for the nNNPDF case an enhancement is observed from 4 to above 20 GeV/c for all systems, with a maximum near 8 GeV/c, clearly not consistent with data. Looking at individual collision systems, EPPS16- and nCTEQ15-based calculations qualitatively, but not quantitatively, capture the general trends. The tension is most clearly visible when comparing the system size dependence. Each nPDF calculation predicts an ordering of the enhancement of R_{xA} in their respective peak region: ^{3}He $+ $Au $> d + $Au $> p + $Au $> p + $Al, which is significant as the systematic uncertainties on the nPDFs within
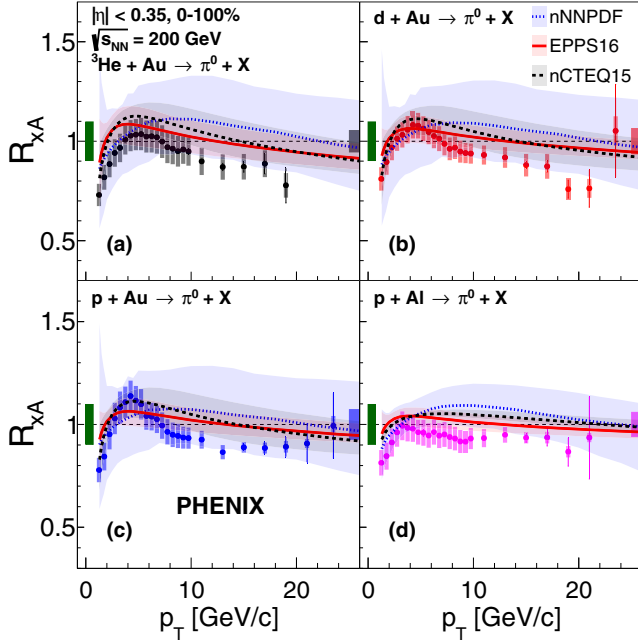
FIG. 11. R_{xA} for inelastic collisions compared to three different nuclear PDF calculations and their uncertainties. The data points include the statistical and systematic uncertainties. The left box around unity represents the overall normalization uncertainty on the $p + p$ collisions and the right box represents the uncertainty from the calculated N_{coll}.
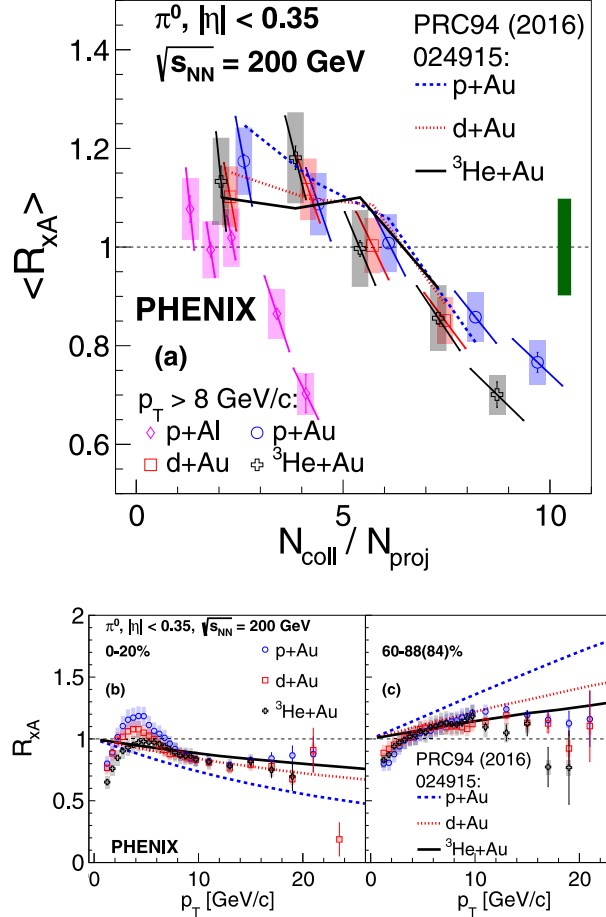

FIG. 12. (a) The $\langle R_{xA} \rangle$ above $p_T = 8 \, \mathrm{GeV}/c$ as a function N_{coll}/N_{proj} with predictions from Ref. [52] for the consequences of high-x nucleon size fluctuations. (b) The R_{xA} as a function of p_T for (b) most-central and (c) most-peripheral collisions.

one approach are highly correlated between systems. The predicted ordering in the lower p_T (2–10 GeV/c) region, depending on the model, results from the modification increasing both with the target size and with the projectile size. In contrast, the data show the reverse ordering $^3\mathrm{He} + \mathrm{Au} < d + \mathrm{Au} < p + \mathrm{Au}$ with decreasing projectile size in the peak region.

For the same reasons that led to predictions of increasing modification at lower p_T, at high p_T, the models predict an ordering of R_{xA} with projectile and target size: $^3\mathrm{He} + \mathrm{Au} < d + \mathrm{Au} < p + \mathrm{Au} < p + \mathrm{Al}$. In contrast, the data show a larger suppression than any of the models, and it is essentially independent of the collision system. However, given the systematic uncertainties on the R_{xA} scale, the nPDF predictions are consistent with the data at high p_T. The different trends, in particular at low p_T, of the nPDF calculations compared to the data suggest that there must be additional physics driving the nuclear modification beyond the nPDFs.

The data show that at high p_T π^0 yields from small systems are suppressed relative to $p + p$ in central event selections, while they are enhanced for peripheral selections. Furthermore, for $p + \mathrm{Au}$, $d + \mathrm{Au}$, and $^3\mathrm{He} + \mathrm{Au}$, the $\langle R_{xA} \rangle$ values for $p_T > 8 \, \mathrm{GeV}/c$ are consistent with a superposition of independent collisions of the projectile nucleons. At the same time, $p + \mathrm{Au}$ and $p + \mathrm{Al}$ show nearly the same $\langle R_{xA} \rangle$ in the same centrality bin selection. These observations contradict any scenarios where parton energy loss would be responsible for the modification, which would necessarily result in an ordering of R_{xA} values as $^3\mathrm{He} + \mathrm{Au} < d + \mathrm{Au} < p + \mathrm{Au} <$

$p + \mathrm{Al} \leqslant 1$ for the system dependence, with the suppression for each system being largest for central and $R_{xA} \approx 1$ for peripheral collisions.

Models that invoke nucleon size variations have been proposed to explain the suppression and/or enhancement pattern seen in the data [33,34]. These models assume that nucleons with high-x partons have a more compact color configuration and thus will produce on average less binary collisions and target participants at the same impact parameter as nucleons without high-x partons. As a consequence, events with a high p_T π^0 would typically be biased toward smaller multiplicity of the overall event, leading to an apparent enhancement in peripheral event selections and a suppression in central events. The calculations from Ref. [52], which predicted jet R_{xA} for $p + \mathrm{Au}$ and $^3\mathrm{He} + \mathrm{Au}$ based on a comparison to $d + \mathrm{Au}$ data,[1] are compared to π^0 $\langle R_{xA} \rangle$ above a p_T of 8 GeV/c [see Fig. 12(a)]. The observed centrality dependence

---

[1]Note that jet R_{xA} presented in Ref. [52] was converted to π^0 R_{xA} assuming $p_T(\pi^0) = 0.7 \, p_T^{\mathrm{jet}} = 0.7 \times 100 \, \mathrm{GeV} \times x_p$ and $\langle R_{xA} \rangle \approx R_{xA}(p_T)$. This procedure was discussed with the authors.

is quite consistent with the data. It can be expected that in this model the same event selection bias would occur in $p + \text{Al}$ collisions.

Although this model plausibly describes the $d + \text{Au}$ and $^3\text{He} + \text{Au}$ data, it particularly misses the $p + \text{Au}$. Additionally, it is important to note that this model predicts an ordering of R_{xA} with system size and centrality at higher p_T. Figure 12 clearly shows that for (b) central collisions the predicted R_{xA} values follow $^3\text{He} + \text{Au} > d + \text{Au} > p + \text{Au}$ and for (c) peripheral collisions the ordering is reversed. In contrast, such an ordering is not supported by the data.

In Ref. [35], the bias of the event selection by centrality occurs because soft particle production away from the hard scattering process is suppressed, caused by the depletion of energy available in the projectile after the hard scattering process. The R_{xA} calculated for $d + \text{Au}$ with this model was consistent with preliminary [35] and final $d + \text{Au}$ data within systematic uncertainties. It would be interesting to see these calculations expanded to the full variety of available data from small systems.

In recent years, particle spectra from $p + p$ collisions at the LHC have been interpreted in the context of hydrodynamic models and the presence of strong radial flow [53–56], but no predictions exist for small systems at RHIC energies that could be compared to the data. If the large anisotropies of particle production seen at RHIC in $p + \text{Au}$, $d + \text{Au}$, and $^3\text{He} + \text{Au}$ are indeed related to hydrodynamic expansion of the collision volume, as suggested in Ref. [27], then the same systems must also exhibit radial flow because the anisotropy would be a geometry driven modulation of radial flow. The effects of radial flow are typically most prominent at p_T below a few GeV/c, where soft particle production mechanisms dominate. In the presence of radial flow, the π^0 yield would be shifted toward higher momentum by the velocity field. Accordingly, when comparing the shape of the π^0 momentum spectra from $x + A$ to that from $p + p$, a depletion of the yield at the lowest p_T is expected, while at higher p_T the yield would be enhanced with a transition near the π^0 mass. Because the p_T range of the π^0 data starts at 1 GeV/c, only the region where an enhancement would be expected can be studied here.

To look for possible indications of radial flow, the integrated yields are calculated for two p_T ranges, 1–2 and 2–3 GeV/c, for all systems and event selections. The results are plotted in Fig. 13 as functions of the charged particle multiplicity density $dN_{\text{ch}}/d\eta$ at midrapidity for the corresponding system and event selection. Also shown on each panel are two lines indicating integrated yields linearly increasing with $dN_{\text{ch}}/d\eta$. The lower line is anchored to the $p + p$ point following a trend of unchanged shape of the spectra, and the upper line matches the yield for the 0–20% $^3\text{He} + \text{Au}$ selection. While the peripheral $p + \text{Al}$ events follow the $p + p$ trend, all other selections show higher integrated yields compared to the $p + p$ trend. Above $dN_{\text{ch}}/d\eta \approx 10$, the data tend to be proportional to $dN_{\text{ch}}/d\eta$ again but at a much higher level.

The observed trend is qualitatively consistent with the presence of radial flow in small systems. Interestingly, the surprisingly rapid transition over the $dN_{\text{ch}}/d\eta$ range from ≈ 3 to 10 is similar to recent observations of low-p_T direct pho-
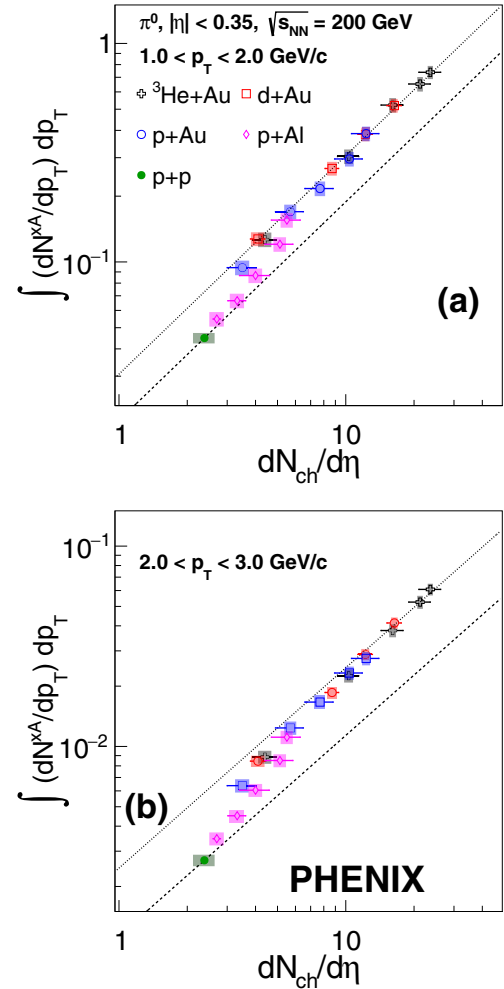

FIG. 13. Integrated yields for (a) 1–2 and (b) 2–3 GeV/c as a function of charged particle multiplicity density at midrapidity. The lines are explained in the text.

ton emission [57] and strangeness production [58]. Both also indicate a transition from $p + p$-like emission to a significant enhancement at similar event multiplicities. Furthermore, the presence of radial flow could naturally explain the much larger observed Cronin effect for protons from small systems [8], which so far has eluded a quantitative understanding. However, before drawing firm conclusions, more investigations are necessary. These should include the study of heavier hadrons, such as kaons and protons.

VII. SUMMARY

In summary, this paper presents measurements of the invariant cross section of neutral pion production from $p + p$ collisions and invariant yields from $p + \text{Al}$, $p + \text{Au}$, $d + \text{Au}$, and $^3\text{He} + \text{Au}$ at $\sqrt{s_{NN}} = 200$ GeV. For $p + p$ the results extend the measured range up to $p_T \approx 25$ GeV/c and improve statistical and systematic uncertainties compared to the previous measurement. NLO pQCD calculations are found to be consistent with the data as previously reported. For $p + \text{Al}$, $p + \text{Au}$, $d + \text{Au}$, and $^3\text{He} + \text{Au}$ collisions at $\sqrt{s_{NN}} =$

200 GeV, π^0 p_T spectra from inelastic collisions and from centrality selected event samples were measured, including a sample of the 0–5% most central events for $p + $ Al, $p + $ Au, and ^{3}He $+$ Au, which was recorded with a dedicated high multiplicity trigger.

At high transverse momentum ($p_T > 8$ GeV/c), where hard scattering processes are the dominant production mechanism, the nuclear modification factors for all collision systems are found to be nearly constant. For the same event selection in percent centrality, different collision systems exhibit a value of R_{xA} that is compatible within uncertainties. For the full inelastic cross section, R_{xA} is consistent with unity, pointing toward little or no nuclear modification of hard scattering processes in small systems. For the most central events, it is observed that R_{xA} is significantly below unity. However, R_{xA} increases monotonically with decreasing centrality and exceeds unity for peripheral collisions. For Au target nuclei, the $\langle R_{xA} \rangle$ above p_T of 8 GeV/c shows a common trend with $N_{\text{coll}}/N_{\text{proj}}$. This indicates that, for hard scattering processes, the nucleons in the small projectile nucleus interact mostly independently with the Au target. For $p + $ Al collisions, $\langle R_{xA} \rangle$ does not follow the same trend. At the same event centrality, the $p + $ Al $\langle R_{xA} \rangle$ is the same as for $p + $ Au, which suggests that the mechanism that causes the change of R_{xA} with centrality does not depend on the target nucleus.

These observations disfavor scenarios where energy loss is a significant contributor to the nuclear modification of high-p_T particle production in small systems. The counterintuitive centrality dependence is likely linked to a mismatch of the centrality selection of events using charged particle multiplicity and mapping them to a number of binary collisions using the standard Glauber model. In this picture, events with a high p_T π^0 are biased toward smaller underlying event multiplicity. This might be due to physical fluctuations of the proton size or simply due to energy conservation if high p_T jets are present.

For lower p_T, R_{xA} for all systems initially increases with p_T and reaches a peak near 4–6 GeV/c for central and semi-central collisions. For peripheral collisions, R_{xA} levels off to a constant at approximately the same high p_T value for all systems. For inelastic collisions and more central collisions, R_{xA} resembles what has been referred to as the Cronin effect in fixed target experiments—a rise, followed by a peak, followed by a plateau. However, unlike at lower energies, $p + p$ and $x + A$ π^0 cross sections are not related by a power $(xA)^{n(p_T)}$ with a common $n(p_T)$. Furthermore, the peak height value around 4–6 GeV/c shows a clear system size dependence $p + $ Au $>$ $d + $ Au $>$ ^{3}He $+$ Au $>$ $p + $ Al, where the R_{xA} peak height value is well above unity for $p + $ Au and drops to close to unity for $p + $ Al collisions.

While the shape of R_{xA} roughly resembles what is expected from the nuclear modification of PDFs, the observed system size dependence of the peak height of R_{xA} shows exactly the reverse ordering of what was predicted by nPDF calculations. Therefore it is likely that nPDFs alone are insufficient to explain the nuclear modifications in small systems.

In the same p_T region, $\langle R_{xA} \rangle$ was used to study the dependence on centrality. For all systems, $\langle R_{xA} \rangle$ in the range 4–6 GeV/c follows a common trend with N_{coll}. At high p_T, $\langle R_{xA} \rangle$ scales with $N_{\text{coll}}/N_{\text{proj}}$ for Au target nuclei, while at lower p_T, $d + $ Au and ^{3}He $+$ Au are not a superposition of $p + $ Au-like collisions. Consequently, different mechanisms must contribute to the nuclear modification at high and low p_T. For high p_T, the apparent centrality dependence is likely due to a bias in the event selection. At lower p_T, final state effects related to the presence of interacting hadrons may be at play. If a QGP droplet is indeed produced during the collision, radial flow may be one possible mechanism to explain this trend, although further investigation is needed that is outside the scope of this paper.

[1] K. Adcox *et al.* (PHENIX Collaboration), Suppression of Hadrons with Large Transverse Momentum in Central Au+Au Collisions at $\sqrt{s_{NN}} = 130$ GeV, Phys. Rev. Lett. **88**, 022301 (2001).

[2] C. Adler *et al.* (STAR Collaboration), Centrality Dependence of High p_T Hadron Suppression in Au + Au Collisions at $\sqrt{s_{NN}} = 130$ GeV, Phys. Rev. Lett. **89**, 202301 (2002).

[3] S. S. Adler *et al.* (PHENIX Collaboration), Nuclear effects on hadron production in $d + Au$ and $p + p$ collisions at $\sqrt{s_{NN}} = 200$ GeV, Phys. Rev. C **74**, 024904 (2006).

[4] J. Adams *et al.* (STAR Collaboration), Evidence from $d + Au$ Measurements for Final State Suppression of High p_T Hadrons in Au + Au Collisions at RHIC, Phys. Rev. Lett. **91**, 072304 (2003).

[5] A. Adare *et al.* (PHENIX Collaboration), Suppression Pattern of Neutral Pions at High Transverse Momentum in Au + Au Collisions at $\sqrt{s_{NN}} = 200$ GeV and Constraints on Medium Transport Coefficients, Phys. Rev. Lett. **101**, 232301 (2008).

[6] B. I. Abelev *et al.* (STAR Collaboration), Neutral pion production in Au + Au collisions at $\sqrt{s_{NN}} = 200$ GeV, Phys. Rev. C **80**, 044905 (2009).

[7] J. W. Cronin, H. J. Frisch, M. J. Shochet, J. P. Boymond, R. Mermod, P. A. Piroue, and R. L. Sumner, Production of hadrons with large transverse momentum at 200, 300, and 400 GeV, Phys. Rev. D **11**, 3105 (1975).

[8] D. Antreasyan, J. W. Cronin, H. J. Frisch, M. J. Shochet, L. Kluberg, P. A. Piroue, and R. L. Sumner, Production of hadrons at large transverse momentum in 200, 300, and 400 GeV $p p$ and $p n$ collisions, Phys. Rev. D **19**, 764 (1979).

[9] J. H. Kuhn, Nucleon number dependence of large transverse momentum reactions and multiple scattering, Phys. Rev. D **13**, 2948 (1976).

[10] M. Lev and B. Petersson, Nuclear effects at large transverse momentum in a QCD parton model, Z. Phys. C **21**, 155 (1983).

[11] X.-N. Wang, Systematic study of high p_T hadron spectra in $p p$, $p A$, and $A A$ collisions from SPS to RHIC energies, Phys. Rev. C **61**, 064910 (2000).

[12] Y. Zhang, G. I. Fai, G. Papp, G. G. Barnafoldi, and P. Levai, High p_T pion and kaon production in relativistic nuclear collisions, Phys. Rev. C **65**, 034903 (2002).

[13] B. Z. Kopeliovich, J. Nemchik, A. Schafer, and A. V. Tarasov, Cronin Effect in Hadron Production Off Nuclei, Phys. Rev. Lett. **88**, 232303 (2002).

[14] A. Accardi and D. Treleani, Minijet transverse spectrum in high-energy hadron nucleus collisions, Phys. Rev. D **64**, 116004 (2001).

[15] I. Vitev and M. Gyulassy, High p_T Tomography of $d + Au$ and Au + Au at SPS, RHIC, and LHC, Phys. Rev. Lett. **89**, 252301 (2002).

[16] D. Kharzeev, Y. V. Kovchegov, and K. Tuchin, Cronin effect and high-p_T suppression in $p A$ collisions, Phys. Rev. D **68**, 094013 (2003).

[17] R. C. Hwa and C. B. Yang, Final State Interaction as the Origin of the Cronin Effect, Phys. Rev. Lett. **93**, 082302 (2004).

[18] V. Khachatryan *et al.* (CMS Collaboration), Observation of long-range near-side angular correlations in proton-proton collisions at the LHC, J. High Energy Phys. 09 (2010) 091.

[19] B. Abelev *et al.* (ALICE Collaboration), Long-range angular correlations on the near and away side in p-Pb collisions at $\sqrt{s_{NN}} = 5.02$ TeV, Phys. Lett. B **719**, 29 (2013).

[20] G. Aad *et al.* (ATLAS Collaboration), Observation of Associated Near-Side and Away-Side Long-Range Correlations in $\sqrt{s_{NN}} = 5.02$ TeV Proton-Lead Collisions with the ATLAS Detector, Phys. Rev. Lett. **110**, 182302 (2013).

[21] S. Chatrchyan *et al.* (CMS Collaboration), Observation of long-range near-side angular correlations in proton-lead collisions at the LHC, Phys. Lett. B **718**, 795 (2013).

[22] A. Adare *et al.* (PHENIX Collaboration), Quadrupole Anisotropy in Dihadron Azimuthal Correlations in Central $d + Au$ Collisions at $\sqrt{s_{NN}} = 200$ GeV, Phys. Rev. Lett. **111**, 212301 (2013).

[23] A. Adare *et al.* (PHENIX Collaboration), Measurements of Elliptic and Triangular Flow in High-Multiplicity ^{3}He + Au Collisions at $\sqrt{s_{NN}} = 200$ GeV, Phys. Rev. Lett. **115**, 142301 (2015).

[24] C. Aidala *et al.* (PHENIX Collaboration), Measurement of long-range angular correlations and azimuthal anisotropies in high-multiplicity $p + Au$ collisions at $\sqrt{s_{NN}} = 200$ GeV, Phys. Rev. C **95**, 034910 (2017).

[25] C. Aidala *et al.* (PHENIX Collaboration), Measurements of Multiparticle Correlations in $d + Au$ Collisions at 200, 62.4, 39, and 19.6 GeV and $p + Au$ Collisions at 200 GeV and Implications for Collective Behavior, Phys. Rev. Lett. **120**, 062302 (2018).

[26] A. Adare *et al.* (PHENIX Collaboration), Measurements of mass-dependent azimuthal anisotropy in central $p + Au$, $d + Au$, and ^{3}He + Au collisions at $\sqrt{s_{NN}} = 200$ GeV, Phys. Rev. C **97**, 064904 (2018).

[27] C. Aidala *et al.* (PHENIX Collaboration), Creation of quark–gluon plasma droplets with three distinct geometries, Nat. Phys. **15**, 214 (2019).

[28] G. Aad *et al.* (ATLAS Collaboration), Transverse momentum and process dependent azimuthal anisotropies in $\sqrt{s_{NN}} = 8.16$ TeV $p + Pb$ collisions with the ATLAS detector, Eur. Phys. J. C **80**, 73 (2020).

[29] A. Adare *et al.* (PHENIX Collaboration), Centrality categorization for $R_{p(d)+A}$ in high-energy collisions, Phys. Rev. C **90**, 034902 (2014).

[30] G. Aad *et al.* (ATLAS Collaboration), Centrality and rapidity dependence of inclusive jet production in $\sqrt{s_{NN}} = 5.02$ TeV proton-lead collisions with the ATLAS detector, Phys. Lett. B **748**, 392 (2015).

[31] A. Adare *et al.* (PHENIX Collaboration), Centrality-Dependent Modification of Jet-Production Rates in Deuteron-Gold Collisions at $\sqrt{s_{NN}} = 200$ GeV, Phys. Rev. Lett. **116**, 122301 (2016).

[32] Z.-B. Kang, I. Vitev, and H. Xing, Effects of cold nuclear matter energy loss on inclusive jet production in $p + A$ collisions at energies available at the BNL Relativistic Heavy Ion Collider and the CERN Large Hadron Collider, Phys. Rev. C **92**, 054911 (2015).

[33] M. Alvioli, B. A. Cole, L. Frankfurt, D. V. Perepelitsa, and M. Strikman, Evidence for x-dependent proton color fluctuations in $p A$ collisions at the CERN Large Hadron Collider, Phys. Rev. C **93**, 011902(R) (2016).

[34] M. Alvioli, L. Frankfurt, D. V. Perepelitsa, and M. Strikman, Global analysis of color fluctuation effects in proton- and deuteron-nucleus collisions at RHIC and the LHC, Phys. Rev. D **98**, 071502(R) (2018).

[35] M. Kordell and A. Majumder, Jets in $d(p)$-A collisions: Color transparency or energy conservation, Phys. Rev. C **97**, 054904 (2018).

[36] A. Adare *et al.* (PHENIX Collaboration), Inclusive cross-section and double helicity asymmetry for π^0 production in $p + p$ collisions at $\sqrt{s_{NN}} = 200$ GeV: Implications for the polarized gluon distribution in the proton, Phys. Rev. D **76**, 051106 (2007).

[37] L. Aphecetche *et al.* (PHENIX Collaboration), PHENIX calorimeter, Nucl. Instrum. Methods Phys. Res., Sect. A **499**, 521 (2003).

[38] R. Brun, R. Hagelberg, M. Hansroul, and J. C. Lassalle, *Geant: Simulation Program for Particle Physics Experiments: User Guide and Reference Manual* CERN-DD-78-2-REV, CERN-DD-78-2, 1978.

[39] S. S. Adler *et al.* (PHENIX Collaboration), A detailed study of high-p_T neutral pion suppression and azimuthal anisotropy in Au + Au collisions at $\sqrt{s_{NN}} = 200$ GeV, Phys. Rev. C **76**, 034904 (2007).

[40] A. Adare *et al.* (PHENIX Collaboration), Pseudorapidity Dependence of Particle Production and Elliptic Flow in Asymmetric Nuclear Collisions of $p + $Al, $p + $Au, $d + $Au, and ^{3}He $+ $Au at $\sqrt{s_{NN}} = 200$ GeV, Phys. Rev. Lett. **121**, 222301 (2018).

[41] B. Alver, M. Baker, C. Loizides, and P. Steinberg, The PHOBOS Glauber Monte Carlo, arXiv:0805.4411.

[42] L. Lyons, D. Gibaut, and P. Clifford, How to combine correlated estimates of a single physical quantity, Nucl. Instrum. Methods Phys. Res., Sect. A **270**, 110 (1988).

[43] A. Valassi, Combining correlated measurements of several different physical quantities, Nucl. Instrum. Methods Phys. Res., Sect. A **500**, 391 (2003).

[44] A. Valassi and R. Chierici, Information and treatment of unknown correlations in the combination of measurements using the BLUE method, Eur. Phys. J. C **74**, 2717 (2014).

[45] B. Jäger, A. Schafer, M. Stratmann, and W. Vogelsang, Next-to-leading order QCD corrections to high-p_T pion production in longitudinally polarized $p p$ collisions, Phys. Rev. D **67**, 054005 (2003).

[46] M. L. Miller, K. Reygers, S. J. Sanders, and P. Steinberg, Glauber modeling in high energy nuclear collisions, Annu. Rev. Nucl. Part. Sci. **57**, 205 (2007).

[47] P. B. Straub, D. E. Jaffe, H. D. Glass, M. R. Adams, C. N. Brown, G. Charpak, W. E. Cooper, J. A. Crittenden, D. A. Finley, R. Gray *et al.*, Nuclear Dependence of High-x_t Hadron

and High-τ Hadron-Pair Production in $p A$ Interactions at $\sqrt{s} = $ 38.8 GeV, Phys. Rev. Lett. **68**, 452 (1992).

[48] R. A. Khalek, J. J. Ethier, J. Rojo (NNPDF Collaboration), Nuclear parton distributions from lepton-nucleus scattering and the impact of an electron-ion collider, Eur. Phys. J. C **79**, 471 (2019).

[49] K. J. Eskola, P. Paakkinen, H. Paukkunen, and C. A. Salgado, EPPS16: Nuclear parton distributions with LHC data, Eur. Phys. J. C **77**, 163 (2017).

[50] K. Kovařík, A. Kusina, T. Jezo, D. B. Clark, C. Keppel, F. Lyonnet, J. G. Morfin, F. I. Olness, J. F. Owens, I. Schienbein, and J. Y. Yu, nCTEQ15: Global analysis of nuclear parton distributions with uncertainties in the CTEQ framework, Phys. Rev. D **93**, 085037 (2016).

[51] D. de Florian, M. Epele, R. J. Hernandez-Pinto, R. Sassot, and M. Stratmann, Parton-to-kaon fragmentation revisited, Phys. Rev. D **95**, 094019 (2017).

[52] D. McGlinchey, J. L. Nagle, and D. V. Perepelitsa, Consequences of high-x proton size fluctuations in small collision systems at $\sqrt{s_{NN}} = 200$ GeV, Phys. Rev. C **94**, 024915 (2016).

[53] T. Bhattacharyya, J. Cleymans, A. Khuntia, P. Pareek, and R. Sahoo, Radial flow in non-extensive thermodynamics and study of particle spectra at LHC in the limit of small $(q - 1)$, Eur. Phys. J. A **52**, 30 (2016).

[54] D. Sarkar, S. Choudhury, and S. Chattopadhyay, Effect of radial flow on two particle correlations with identified triggers at intermediate p_T in p-Pb collisions at $\sqrt{s_{NN}} = 5.02$ TeV, Phys. Lett. B **760**, 763 (2016).

[55] Y. Hirono and E. Shuryak, Femtoscopic Signature of strong radial flow in high-multiplicity pp collisions, EPJ Web Conf. **141**, 01008 (2017).

[56] A. Khuntia, H. Sharma, S. Kumar Tiwari, R. Sahoo, and J. Cleymans, Radial flow and differential freeze-out in proton-proton collisions at $\sqrt{s} = 7$ TeV at the LHC, Eur. Phys. J. A **55**, 3 (2019).

[57] A. Adare *et al.* (PHENIX Collaboration), Beam Energy and Centrality Dependence of Direct-Photon Emission from Ultrarelativistic Heavy-Ion Collisions, Phys. Rev. Lett. **123**, 022301 (2019).

[58] J. Adam *et al.* (ALICE Collaboration), Enhanced production of multi-strange hadrons in high-multiplicity proton-proton collisions, Nat. Phys. **13**, 535 (2017).